Impact of Trailing Edge Overhang Length on the Loss Characteristics of Fully Cooled Transonic Nozzle Guide Vanes

Daniel Burdett
Department of Engineering Science,
University of Oxford,
Oxford OX2 0ES, UK
e-mail: daniel.burdett@univ.ox.ac.uk

Thomas Povey[1]
Department of Engineering Science,
University of Oxford,
Oxford OX2 0ES, UK
e-mail: thomas.povey@eng.ox.ac.uk

The trailing edge (TE) design of a cooled high-pressure (HP) nozzle guide vane (NGV) requires consideration of both cooling and aerodynamic performances. Two designs are in common use: the centered-ejection design, in which coolant is ejected through a slot in the TE with roughly symmetrical suction-side (SS) and pressure-side (PS) TE tips; and the SS-overhang design, in which the SS and PS TE tips are staggered. This second design has been favored in recent years because it has been presumed to be aerodynamically advantageous. In this article, we re-examine this assumption by studying a parametric design set between these two design extremes. We do this using extensive high-fidelity experimental measurements performed at engine-scaled conditions (matched Mach number, Reynolds number, and coolant-to-mainstream pressure ratio) on a full-annular cascade of real engine parts. To provide insight into the mechanisms affecting loss, we use complementary unsteady computational fluid dynamics (CFD) simulations. We analyze the changes in the flow structure, local loss coefficient distribution, wake mixing rate, average profile loss coefficient, and base pressures. [DOI: 10.1115/1.4056056]

Keywords: boundary layer development, computational fluid dynamics (CFD), fluid dynamics and heat transfer phenomena in compressor and turbine components of gas turbine engines, measurement techniques, turbine blade and measurement advancements, turbomachinery blading design, vortex shedding

Introduction and Literature Review

High turbine inlet temperatures necessitate cooling of the high-pressure (HP) nozzle guide vane (NGV). Most HP NGVs use both internal (impingement, pedestal/fin banks, etc.) and film cooling. The cooling comes with an aerodynamic and thermodynamic penalty to the cycle. The trailing edge (TE) overhang is exposed and cannot be internally cooled and is therefore particularly reliant on good film coverage. This is normally achieved through ejecting coolant from the trailing part of the vane through a TE slot. The region immediately downstream of the TE is one of relatively low static pressure (on account of flow acceleration) and total pressure (separated flow), which is favorable in terms of the pressure drop offered across the internal system. There are two common design variants for the cooled TE: *centered-ejection*, and *suction-side (SS)-overhang* (also commonly called *pressure-side (PS)-cutback*). The centered-ejection design has an approximately symmetric centered slot, in which both the PS and SS TE tips have the advantage of being both internally and film cooled. However, this comes with the aerodynamic penalty of a thicker TE. In the *SS-overhang* design, the SS TE tip extends further in the chordwise direction than the PS TE tip (it overhangs). This offers the advantage of a thinner (ultimate) TE, but at the cost of increased cooling requirement for the overhanging length. Detailed consideration of the impact of TE overhang length on cooling requirement is beyond the scope of this article and is worthy of its own study.

At transonic conditions, there is a complex interaction among the TE slot coolant flow, the TE shock structure, the separated base region, and the development of the downstream free shear layers. The loss generated in this region typically accounts for about a third of total profile loss of the NGV [1]. Aerothermal optimization of this region is therefore important.

Most early cooled TE designs had a centered-ejection design. More recent engine designs have favored SS-overhang geometries because of the supposed aerodynamic advantages of the thinner (ultimate) separated TE region (often called *base region*). However, the literature is not in consensus on this point, as we demonstrate in the following review. To confuse matters further, there is more recent evidence that suggests that shorter overhangs may offer both aerodynamic and thermal advantages at low-transonic Mach numbers. This has become more relevant as designers consider the possibility of twin-HP turbines, with HP NGV exit Mach numbers in the range 0.8–0.9 (compared to the typical value of 0.95).

The lack of consensus in the existing literature is our primary motivation for more carefully re-examining the impact of TE design. We take advantage of high technology readiness level (TRL) experimental data using fully cooled engine parts operated at non-dimensionally engine-representative conditions. A secondary motivation is to clarify the penalty (or otherwise) associated with deliberate removal of TE material as part of the repair process of damaged in-service components.

Early studies of TE loss focused on the sensitivity to TE thickness in uncooled vanes [2,3]. The first studies of cooled TE geometries were those of Whitney et al. [4] and Prust and Bartlett [5,6], who tested centered-ejection designs with different TE and slot thicknesses at a range of coolant-to-mainstream mass flow ratios. These early results presented row efficiency as a function of coolant-to-mainstream mass flow ratio and found that, in most cases, efficiency rose significantly with the mass flow ratio. The exception was for very narrow slots with mass flow ratios below 1.0%, where a minimum efficiency condition was seen. The change in efficiency arose due to a combination of the kinetic energy (KE) of the coolant jet in relation to that of the mainstream

---

Journal of Turbomachinery MAY 2023, Vol. 145 / **051012-1**

and also the impact of coolant flow on TE loss (affecting the base pressure distribution and the effective TE blockage). At mass flow ratios below approximately 2.0%, the KE of the coolant jet was low, and the latter effect was relatively strong, producing higher efficiency from wider slot designs, whereas for mass flow ratios above 2.0%, the former effect was dominant and narrower slots performed better. The positive impact of high coolant KE on efficiency was conflated by the fact that the efficiency definition took no account of the coolant flow in setting the ideal reference flow. This problem was addressed in more recent studies by including the coolant energy input in the definitions of efficiency and loss coefficient.

Sieverding [7] studied the impact of TE coolant ejection from a central slot on base pressure in the transonic regime. The coolant jet split the base region into two sections of significantly different base pressure (by typically 3% of the mean base pressure). The base pressure asymmetry was attributed to a small misalignment between the slot exit angle and the direction of the wake path (classical deviation effect). As the coolant-inlet-pressure-to-base-pressure-ratio increased from 1.00 to 1.48, average base pressure increased to a maximum value 11.9% above the uncooled base pressure, before gradually falling as the injection pressure ratio was increased further. To the extent that we can take base pressure as a proxy for TE loss (it is a good measure of the pressure drag, but does not account for mixing losses between the mainstream and TE coolant flows or the KE introduced by the coolant, so the analogy is only partial), the maximum base pressure condition is expected to be associated with (though not exactly coincident with) a minimum loss coefficient.

There are many studies in the literature (e.g., Refs. [8–13]) of the impact of varying TE coolant flowrate (expressed as a coolant-to-mainstream mass flux ratio, velocity ratio, or blowing ratio) on aerodynamic loss for both centered-ejection and SS-overhang type TE designs. Defining a KE loss coefficient so as to account for the energy input of coolant flow, all of these studies show that loss coefficient first decreases (with respect to the uncooled condition) with the introduction of TE coolant flow, with a minimum value of loss coefficient at moderate mass flux, velocity, or blowing ratio, and then increases again for higher ratios. Acknowledging the caveats noted earlier for the analogy between TE loss and base pressure, this result is in line with that of Sieverding [7], who showed a maximum base pressure at a moderate coolant flowrate.

Raffel and Kost [9] used Schlieren imaging and particle image velocimetry (PIV) methods to visualize and understand the influence of TE coolant ejection on the TE shock structure. To do this, they used a simplified flat plate working section designed to replicate the flow structures in the vicinity of the TE of an NGV cascade. They operated at a Mach number of 1.27. The introduction of a moderate TE coolant flow ($\dot{m}_c/\dot{m}_m = 0.5–1.0\%$) resulted in each of the oblique shockwaves on either side of the TE each being replaced by a pair of weaker oblique shocks. The change in the TE shock structure reversed at higher coolant mass flowrates ($\dot{m}_c/\dot{m}_m = 1.5–2.5\%$).

Several authors have directly compared the loss produced by different cooled TE geometries, and these are now briefly reviewed. In 1985, Kost and Holmes [8] experimentally compared TE geometries with a central slot and with film rows close to the TE, at a Mach number of 1.15. The latter design provides a thinner ultimate TE (akin to a modern SS-overhang design) and surface film coverage near the TE. The centered-ejection design had 76.2% higher loss coefficient (expressed as a percentage of the film-cooled TE loss coefficient) at the zero coolant flow, due to having its ultimate TE thickness being approximately 2.7 times greater to accommodate the internal slot. However, as the coolant-to-mainstream mass flow ratio increased from 0% to 3.5%, the percentage difference in loss coefficient between the two designs fell to 11.2%. That is, the reduction in loss coefficient with TE ejection was significantly greater for the centered-ejection design.

In 1994, Kapteijn et al. [14] compared centered-ejection and SS-overhang TE geometries for Mach numbers ranging from 0.7 to 1.2. At zero coolant flowrate and Mach number 1.1, Schlieren images showed a distinct shockwave originating at the PS TE lip, in addition to the normal shock-pair at the TE, which was observed for both TE designs. The PS-lip shock was suppressed by a moderate TE coolant flow (coolant flow reduces the effective step height at the PS-lip). At subsonic conditions, the loss coefficient of the SS-overhang design was approximately 24% higher than the centered-ejection design. Direct comparison is difficult because neither the overall thickness of the ultimate TE (42% higher for centered-ejection design) nor the minimum metal thickness (25% higher for SS-overhang design) was matched between the designs. As the Mach number passed unity, both designs showed a rapid rise in the loss coefficient and the difference between them grew to approximately 36%. This increase was attributed to shock–boundary layer interaction caused by the PS-lip shock.

In 2001, Uzol and Camcı [15] experimentally compared centered-ejection and SS-overhang TE designs (with equal minimum metal thicknesses) at four different coolant-to-mainstream mass flow ratios at subsonic conditions. PIV measurements showed that the SS-overhang design gave both a shallower and more asymmetrical wake (more gradual velocity profile decay on the PS), and a 16% lower total pressure loss coefficient than the centered-ejection design. The variation in the total pressure loss coefficient with mass flow ratio was in accord with Refs. [8–13] for both TE designs, although the magnitude of the sensitivity was considerably higher for the SS-overhang design than the centered-ejection. This was attributed to the effect of the changing mass flow ratio on the effective height of the surface discontinuity at the PS lip and consequently on deviation of the PS mainstream flow.

In 2012, Rehder [12] experimentally compared centered-ejection and SS-overhang TE designs in a linear cascade, using coolant-to-mainstream mass flow ratios in the range 0–2% and Mach numbers 0.9 and 1.2. In this comparison, the ultimate TE thickness of the SS-overhang design had the same thickness as that of the *entire* centered-ejection design, giving more than double the minimum metal thickness for the SS-overhang design. Although this led to one sort of like-for-like comparison, it is unrepresentative of engine design constraints. At a Mach number of 0.9, the SS-overhang design produced approximately 50% higher loss coefficient than the centered-ejection at a mass flow ratio of 0.5% and up to 200% higher at 2.0% mass flow ratio. The authors consider the interaction between mainstream and coolant flows in the separated region downstream of the PS lip as a possible explanation for the performance difference, but the larger overall thickness of the SS-overhang design (including the PS lip) may also have been responsible for some of the difference.

In 2016, Wang et al. [13] presented perhaps the most comprehensive computational study of cooled TE designs in the literature to date. They used 2D Reynolds-averaged Navier–Stokes (RANS) to study a typical HP rotor geometry with a SS-overhang TE design, at a Mach number of 1.2. They compared five different SS-overhang lengths (between 6% and 14% of tangential chord) at coolant-to-mainstream mass flow ratios between 0% and 6%. The ranking of different overhang lengths in terms of loss coefficient depended on mass flow ratio. At mass flow ratios below 2%, overhang lengths of 10–12% tangential chord provided the lowest loss coefficient, while for higher mass flow ratios (above approximately 3%), the optimum overhang length fell to 6–8% of tangential chord. The overhang length affected the entire cascade aerodynamics, primarily through influencing the TE shock structure.

In 2018, Melzer [16] experimentally studied the impact of TE vortex shedding in the transonic regime, noting periodic shock generation in phase with the shedding of vortices from the TE. Both centered-ejection and SS-overhang designs were studied, with equal minimum metal thicknesses in all cases, over a Mach number range 0.4–1.0. In the transonic range, the unsteady flow behavior varied significantly with the TE blowing ratio. At blowing ratios up to around 0.3, vortices were shed from the entire width of the separated *base region*. A long overhang length

(approximately 6.0% of tangential chord) was able to suppress the vortex shedding even in the absence of cooling, producing a reduction in loss coefficient of up to 43% relative to TE designs that did not suppress vortex shedding. Moderate blowing ratios (in the range 0.3–0.7) suppressed vortex shedding in all TE designs, with loss coefficients within ±22% of each other. At blowing rates above approximately 0.7, there was a transition in the structure of vortex shedding to vortices being shed from the individual SS and PS TE tips, in most cases. An exception to this was seen for a short overhang length (approximately 1.5% of tangential chord), for which the vortices shed from the two TE tips coalesced into a single vortex street. This effect was associated with an increase in the loss coefficient of up to 43% relative to shedding from the two separate tips. Differences in vortex shedding in the transonic regime (as described earlier) were the only significant source of differences in the sensitivity of loss coefficient to Mach number between TE geometries. These results demonstrate the high sensitivity of TE loss in the transonic range to TE vortex shedding behavior and illustrate the importance of employing an unsteady numerical method to predict TE loss.

In a closely associated study, Melzer and Pullan [16,17] investigated a number of different uncooled TE shapes (round, square, elliptical) and demonstrated the role that vortex shedding in the transonic regime plays in determining TE loss. They showed that square TE designs limited the extent of vortex shedding (when compared to round TEs) at Mach numbers above around 0.8. This led to the square TE having approximately 8% lower loss coefficient than the round TE, opposite to their loss ranking at low-subsonic conditions.

Taking the literature as a whole, we see a number of comparisons of particular SS-overhang and centered-ejection designs, and some parametric studies of different overhang lengths. In many cases, however, the designs were not equivalent in terms of TE thickness, TE slot width, etc., and very little attempt has been made in previous studies to correct for such dissimilarities. In part, this problem is inherent, in that direct equivalents (between SS-overhang and centered-ejection) might not be easy to clearly define. Broadly, the data suggest that when designs are normalized by minimum metal thickness (such that similar thermal and mechanical duty might be expected), an SS-overhang design might be favored over centered-ejection. Comparisons of different overhang lengths show that the optimum overhang length from an aerodynamic perspective is dependent on the entire cascade aerodynamic field, which is—in turn—partly dependent on the unsteady behavior of the wake. The unsteady behavior is difficult to accurately predict, further justifying the necessity of detailed experimental aerodynamic measurements in a high-TRL environment.

The purpose of this study is to fill a gap in the literature, by performing a very detailed analysis of loss characteristics for a series of well-defined cooled TE designs of varying SS-overhang length, constrained by achievable manufacturing limits. The four TE designs we study form a parametric set between a pure centered-ejection design and SS-overhang design (up to 6.3% of tangential chord). A full-annular ring of fully cooled engine parts were used for the study, which was conducted at engine-representative conditions of Mach number, M_2, Reynolds number, Re, and coolant-to-mainstream pressure ratio, p_{0c}/p_{0m}. The study was performed in the high-TRL Engine Component AeroThermal (ECAT) facility [18] at the University of Oxford. Experimental results are compared to unsteady Reynolds-averaged Navier–Stokes (URANS) predictions. The performance of the four TE designs is assessed in terms of average profile loss coefficient values, local loss coefficient distributions, and wake mixing rates. Fundamental mechanisms responsible for the observed effects are discussed.

Overview of Experimental Facility

Experiments were performed in the ECAT facility [18], a high-TRL blowdown annular cascade. For the experiments performed for the current study, the facility was built with HP NGVs

from a modern civil turbofan engine. The same set of vanes was used for the entire test campaign, with geometry variation achieved by sequential machining of the TE. Tests were conducted at engine-representative conditions of M_2, Re (based on tangential chord length), and p_{0c}/p_{0m}. Test conditions are summarized in Table 1. The mass flow ratio between TE coolant and mainstream flows was approximately 0.02 in all tests. The TE-to-mainstream blowing ratio (the product of the mass flow ratio and the nominal passage-to-TE slot area ratio) was approximately 0.53.

An overview of the facility operation and its general capabilities is presented in Ref. [18]. A description of the working section instrumentation and associated uncertainty analysis is presented in Ref. [19], and the traverse measurement process, and analysis of aerodynamic loss measurement capabilities, is presented in Ref. [20]. These details are not repeated in this article. Figure 1 shows a cross section schematic of the NGV ring and measurement planes.

Independently (of the mainstream) metered coolant air is fed from both the hub and the case (see Fig. 1), allowing coolant-to-mainstream pressure ratio to be maintained to within approximately ±0.02%. The vane has both film cooling and TE slot cooling. Upstream of the TE slot, coolant air passes through a row of ribs aligned normal to the flow direction. This results in a non-uniform coolant distribution at ejection from the TE slot [20]. Tests were performed at a nominal coolant-to-mainstream temperature ratio of unity. The previous literature (e.g., Refs. [7,21]) suggests that the sensitivity of loss coefficient to coolant-to-mainstream density ratio is minimal for fixed momentum flux

Table 1 Test operating conditions in the ECAT facility

| Parameter	Nominal value
No. of vanes	40
Vane inlet total pressure, p_{0m} (bar)	2.00 bar
Vane inlet total temperature, T_{0m} (K)	290 K
Vane inlet turbulence intensity, Tu (%)	6–10%
Vane pressure ratio, p_2/p_{0m} (–)	0.54
Vane exit Mach number, M_2 (–)	0.97
Vane exit Reynolds number, Re (–)	1.6×10^6
Coolant-to-mainstream pressure ratio, p_{0c}/p_{0m} (–)	1.025
Coolant-to-mainstream temperature ratio, T_{0c}/T_{0m} (–)	1.00
Trailing edge-to-mainstream mass flow ratio, $\dot{m}_{TE}/\dot{m}_m$ (–)	0.02
Trailing edge-to-mainstream blowing ratio, $\rho_{TE} v_{TE}/\rho_m v_m$ (–)	0.53
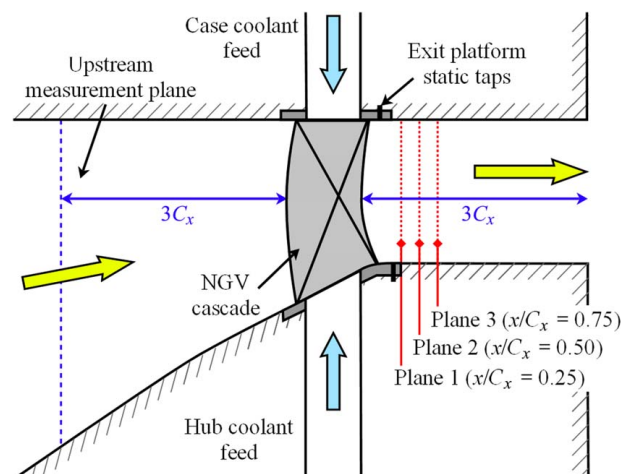
Fig. 1 Schematic of the NGV ring and measurement planes

ratio. Tests were performed at an exit Mach number of $M_2 = 0.97$ (typical variation of $\pm 0.14\%$ of the target value).

Instrumentation and Measurement Process

Vane inlet total pressure, p_{0m}, and total temperature, T_{0m}, were measured at an upstream measurement plane three axial chord lengths upstream of the cascade leading edge, using four fixed pitot rakes and four fixed thermocouple rakes, each with eight measurement points distributed over the vane span (32 measurements each of p_{0m} and T_{0m}). Vane exit static pressure was measured on the hub and case vane exit platform extent (see Fig. 1), at 0.17 C_x downstream of the TE. Six vanes (from the total of 40) were instrumented with platform tappings (total of 84 tappings across the six vanes). The cascade operating pressure ratio was taken as the ratio of mean-exit-static to mean-inlet-total pressure. The bias and precision uncertainties in vane pressure ratio were estimated as $\pm 0.365\%$ and $\pm 0.007\%$ to 95% confidence, respectively. A detailed uncertainty analysis is presented in Ref. [19].

Traverse measurements were conducted in three axial planes using a two-axis (radial-circumferential) hub-mounted traverse gear. Details of the traverse equipment are given in Ref. [18]. The three traverse planes (planes 1, 2, and 3, marked in Fig. 1) were located ¼, ½, and ¾ of axial chord downstream of the TE plane. Measurements were made using a five-hole pneumatic pressure probe, with a tip diameter of 2.8 mm and a single-hole pitot probe (for near-wall measurements) with a diameter of 0.8 mm. Further details of the probes are given in Ref. [20]. The five-hole probe was calibrated over a Mach number range $0.3 \leq M \leq 1.4$, to allow evaluation of total and static pressures, Mach number, and yaw and pitch angles.

Full area surveys in each of the three traverse planes were conducted over a circumferential range of 2.5 vane pitches (including two complete wakes) and a radial range of approximately 3–97% of span. Wakes from the same two vanes were tracked between the three axial planes by changing the circumferential traverse limits. The probes were traversed slowly in a pattern of circumferential sweeps in alternating directions, with radial spacing of 1.4 mm. The frequency response of the probe-transducer system was estimated as 120 Hz. An impulse response deconvolution technique [22] was used to improve the frequency response to approximately 720 Hz, without compromising the fidelity of the underlying signal. The resulting spatial resolution of traverse data in the circumferential direction (at midspan) was 0.08 mm.

Loss Coefficient Definitions

We quantify aerodynamic loss using a KE loss coefficient, ζ, defined by

$$\zeta = 1 - \eta = 1 - \frac{v_2^2}{v_{2s}^2} = 1 - \frac{1 - \left(\frac{p_2}{p_{02}}\right)^{\chi}}{1 - \left(\frac{p_2}{p_{01}}\right)^{\chi}} \tag{1}$$

where the vane efficiency, η, is defined as the ratio of actual exit KE to ideal exit KE, v_2 is the measured exit flow velocity, v_{2s} is the isentropic exit velocity, and $\chi = (\gamma - 1)/\gamma$.

In this article, we use four representations of loss coefficient: a *local KE loss coefficient* to present full area survey data at particular axial planes; a *circumferentially-averaged KE loss coefficient* to present radial distributions of loss; a *plane-averaged KE loss coefficient* value as a summary of *already manifest loss*; and a *fully mixed-out KE loss coefficient* as a summary of *unavoidable loss*. These definitions are discussed in detail in Ref. [20]. We now briefly re-iterate the definitions. From Eq. (1), we define the *local KE loss coefficient* as follows:

$$\zeta'(r, \theta) = 1 - \frac{1 - \left(\frac{p_2(r, \theta)}{p_{02}(r, \theta)}\right)^{\chi}}{1 - \left(\frac{p_2(r, \theta)}{p_{01}}\right)^{\chi}} \tag{2}$$

where r and θ denote radial and circumferential positions, respectively. From Eq. (2), we define the circumferential-average KE loss coefficient (at a specific radius) by replacing the local variables $p_2(r, \theta)$ and $p_{02}(r, \theta)$ with a circumferentially area-averaged static pressure, $\overline{p_2}(r)$, and a circumferentially mass-flux-averaged total pressure, $\overline{p_{02}}(r)$, respectively (choice of weighting method for circumferential and plane-average total pressures is examined in detail in Ref. [23]) giving

$$\zeta''(r) = 1 - \frac{1 - \left(\frac{\overline{p_2}(r)}{\overline{p_{02}}(r)}\right)^{\chi}}{1 - \left(\frac{\overline{p_2}(r)}{p_{01}}\right)^{\chi}} \tag{3}$$

We define the plane-averaged KE loss coefficient as follows:

$$\zeta''' = 1 - \frac{(\dot{m}_m + \dot{m}_c)\left[1 - \left(\frac{\overline{p_2}}{\overline{p_{02}}}\right)^{\chi}\right]}{\dot{m}_m\left[1 - \left(\frac{\overline{p_2}}{p_{01}}\right)^{\chi}\right] + \dot{m}_c\left[1 - \left(\frac{\overline{p_2}}{p_{0c}}\right)^{\chi}\right]} \tag{4}$$

where $\overline{p_2}$ is the area-weighted average static pressure, $\overline{p_{02}}$ is the mass-flux-weighted average total pressure, and $\dot{m}_m$ and $\dot{m}_c$ are the mainstream and coolant mass flowrates, respectively.

Finally, we define the mixed-out average KE loss coefficient as follows:

$$\zeta'''' = 1 - \frac{(\dot{m}_m + \dot{m}_c)\left[1 - \left(\frac{\overline{p_2}'}{\overline{p_{02}}'}\right)^{\chi}\right]}{\dot{m}_m\left[1 - \left(\frac{\overline{p_2}'}{p_{01}}\right)^{\chi}\right] + \dot{m}_c\left[1 - \left(\frac{\overline{p_2}'}{p_{0c}}\right)^{\chi}\right]} \tag{5}$$

where $\overline{p_2}'$ and $\overline{p_{02}}'$ are the *mixed-out* average static and total pressures. These values are determined using the method of Dzung [24], in which the properties of the mixed-out flow are calculated at a single, swirl-averaged radius (i.e., the radius at which swirl velocity has its average value).

Trailing Edge Geometries

Figure 2 shows a diagram of the four TE geometries that were tested. We refer to these as Geometry 1 to Geometry 4. The designs form a systematic parametric set with SS-overhang lengths: 6.3%, 4.2%, 2.1%, and 0.0% of tangential chord (we define tangential chord as the circumferential distance between the leading edge and trailing edge extremes of the NGV meanline section). The geometries were formed on the same set of parts by sequential machining back of the SS TE. To achieve similarity between the SS TE tips of all geometries, the SS TE tips of Geometries 2, 3, and 4—which were initially machined to a square-edge—were hand-dressed to approximate the rounded shape of Geometry 1. The unique construction of the ECAT facility allows this operation to be performed without any movement of the NGV ring (see Ref. [25]).

The impact of TE shape on TE loss was examined by Melzer and Pullan [17], the key effect being a change in the location of the shear layer separation point. While rounded TEs generally offer lower loss coefficient at low-subsonic conditions (Mach numbers below around 0.8), some square TEs were shown to have a preferential vortex shedding structure in the transonic regime, with lower overall loss coefficient.

The SS TE thickness, t_{SS}, changed as overhang length was reduced due to the taper in the engine part. Table 2 summarizes
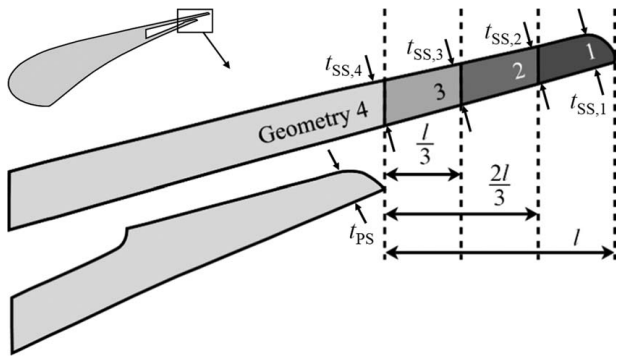
Fig. 2 Diagram showing the vane (top left) and a magnified view of the four TE geometries. The SS-overhang length for Geometry 1 is marked *l*.

Table 2 Summary of SS TE tip thicknesses and axial chord lengths for each geometry

Geometry	1	2	3	4
t_{SS}/mm	0.559	0.603	0.667	0.720
$t_{SS}/t_{SS,1}$	1.000	1.078	1.193	1.288
C_x at 25% span/mm	30.99	30.87	30.57	30.32
C_x at 50% span/mm	29.84	29.74	29.50	29.31
C_x at 75% span/mm	30.35	30.25	30.03	29.85

the SS TE thicknesses for each geometry, along with their axial chord lengths at three spanwise positions. t_{SS} rose by +28.8% between Geometries 1 and 4. This is a necessary artifact of the way the test was set up (to preserve exact similarity between the geometries in all other respects) and is accounted for in the analysis that follows.

Numerical Method

URANS simulations of all TE geometries were performed using ANSYS CFX. Melzer [16] showed that changes in vortex shedding behavior play a key role in determining the influence of TE geometry on loss coefficient. This was the primary motivation for performing unsteady simulations in this work. Steady and unsteady RANS simulations of engine part NGV performance are compared in detail in Ref. [20], and URANS is shown to provide a slightly improved match with experimental data. The domain was a rotationally periodic annular sector of two vane passages. This is shown in Fig. 3(a). An octree-based mesh was generated using BOXERmesh. A midspan cross section (Geometry 1) is shown in Fig. 3(b). The mesh was moderately refined in the paths of the wake centers and strongly refined very close to the TE. Figure 3(c) shows close-up views of the near-TE mesh for each of the four TE geometries. Care was taken to ensure that changes in the mesh between geometries were limited to the immediate vicinity of the SS TE tip. A grid sensitivity study was conducted to ensure the results were independent of grid density. Grids with total cell counts of 18, 33, and 57 million cells, but the same relative refinement arrangements, were compared. Results convergence was assessed based on flow capacity, and local distributions of velocity, total, and static pressure. The finest mesh (57 million cells) was used for the final study. The solver was second-order discretized and density based. The shear stress transport (SST) k-ω model was used model was used for turbulence closure.

At the main inlet boundary, uniform conditions of total pressure, total temperature, and turbulence intensity were specified, matched to the experimental conditions (Table 1). The annulus lines of the inlet duct between the inlet boundary and the NGV leading edge
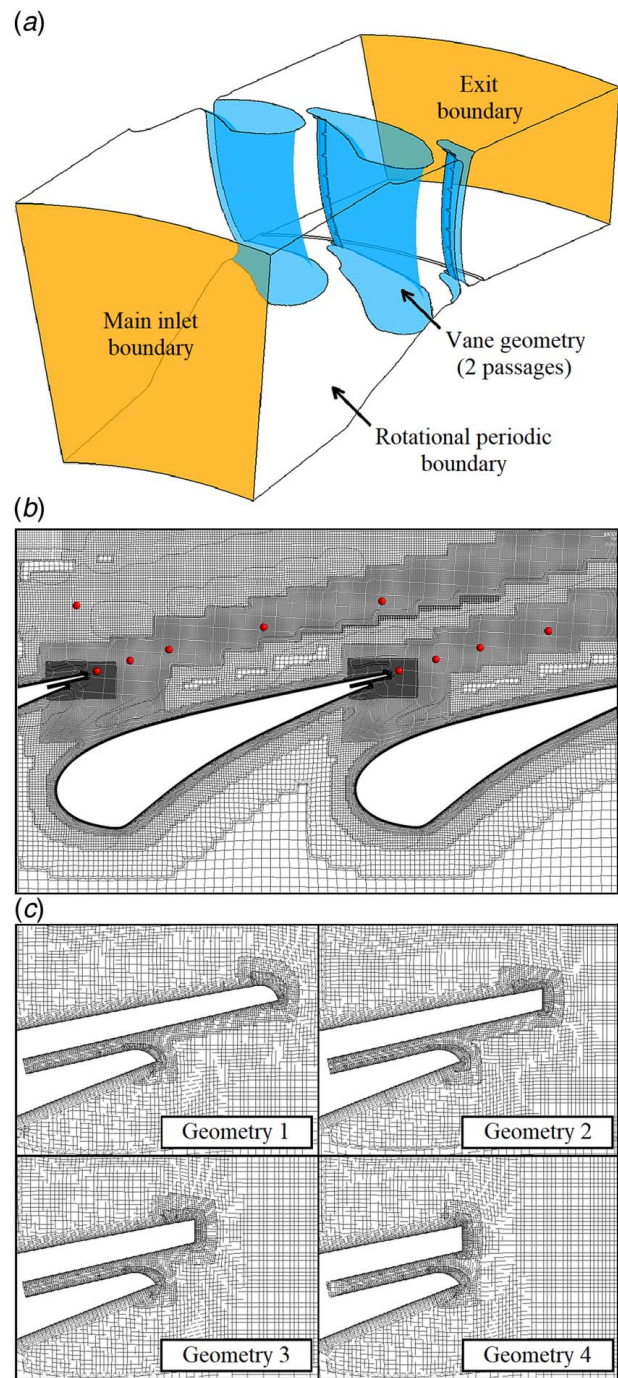

Fig. 3 (a) CFD geometry, (b) midspan mesh cross section for Geometry 1, and (c) near-TE mesh detail for all geometries

were matched to the ECAT facility, so that the spanwise profile of the flow radial angle approaching the cascade was closely matched to the experiment. At the exit boundary, an area-average static pressure was specified, with the requirement to satisfy radial equilibrium. The exit pressure was set in the following iterative manner: the computational fluid dynamics (CFD)-predicted static pressure field at the nominal pressure ratio was interrogated at the locations of the hub and case platform static tappings (see Fig. 1), and a mean vane pressure ratio was evaluated; this was compared to the nominal experimental value; the exit static pressure was then adjusted to achieve a better match and the CFD re-run. This process was repeated until a high level of convergence was reached, ensuring precise matching of the vane pressure ratio between CFD and experiment.

The accuracy of the source-terms film cooling model is considered in detail in Ref. [20]. Resolving individual film cooling holes in the CFD geometry would likely be significantly more accurate; however, the additional computational expense was not considered to be justified for studying performance differences between TE geometries.

Film cooling (210 holes per vane in 11 rows) was simulated using source-terms with a specified mass flowrate and direction vector. Mass flowrates for each *row* were established from the cooling system design for the component, which is a sophisticated network analysis with potential field model. A single-scale factor (close to unity) was then applied to all *row* mass flows to match the total coolant capacity to that measured in the experiment. The individual *hole* mass flowrates were estimated using the CFD-predicted local surface static pressure distribution (evaluated from preliminary uncooled CFD results) and area-scaled nominal capacity characteristics for each hole, constrained so the particular row mass flowrate was satisfied. Individual hole mass flowrates were used as the boundary conditions in the CFD.

The TE slot was fully resolved, with a mass flow inlet boundary eight slot widths upstream of the slot outlet (see Fig. 3). The mass flowrate was established by the same process as the film row mass flows, described earlier. The TE slot inlet boundary was split into seven separate sections along the vane span, separated by six elliptical cutouts matched to the TE shapes of the internal ribs in the experimental vanes. This was designed to simulate the coolant flow development, and therefore, the non-uniform coolant distribution, at ejection into the external flow. Further details of the geometry can be found in Ref. [20].

For each TE geometry, simulations were first converged as steady solutions. These results were then used to initialize the unsteady calculations. A time-step of one tenth of the estimated TE vortex shedding period was used, with solutions run until the equation residuals were converged to within 10^{-6}. We also required that solution values at strategically located monitor points in the wake region were converged to approximately periodic fluctuations. Solutions were then time-averaged over the last 20 shedding periods (an averaging period of 4.6×10^{-4} s).

Unsteady Behavior of Numerical Results

The unsteady behavior predicted by URANS for each TE geometry was analyzed by inspecting the temporal variation of the pressure field at a number of monitor points in the wake (marked in Fig. 3(b)). The non-dimensional magnitude (defined as the root-mean-square (RMS) value of the periodic signal, expressed as a percentage of the local time-mean isentropic dynamic head) and non-dimensional frequency (expressed as a Strouhal number, St, based on the mean exit flow velocity and the TE thickness) of periodic static pressure fluctuations in the wake flow for each TE geometry at three spanwise locations are plotted in Fig. 4. The midspan data are also summarized in Table 3.

For each geometry, the Strouhal numbers were in reasonably good agreement at the three spanwise locations, with St varying by no more than 0.02 across the span. The St values range from 0.20 to 0.32 between geometries. This is in reasonable agreement with a cylinder in crossflow which, for the same Reynolds number, has a characteristic Strouhal number of approximately 0.23 [26]. For Geometries 1–3, the magnitude of normalized pressure fluctuations was very low, in the range 0.06–0.13% of local isentropic dynamic head ($p_{01} - \bar{p}$, where $\bar{p}$ is the temporal mean of the unsteady pressure signal). In contrast, the normalized pressure fluctuation for Geometry 4 was approximately 0.80%, or 8.0 times larger than the average for Geometries 1–3. The magnitude of fluctuations at 75% span for Geometry 4 is approximately half that at 25% and 50% span. This is thought to be due to a Mach number dependence of the shedding for Geometry 4 (reduced Mach number toward the case).

The increase in the magnitude of pressure fluctuations for Geometry 4 is thought to be caused by a change in the shedding mode as
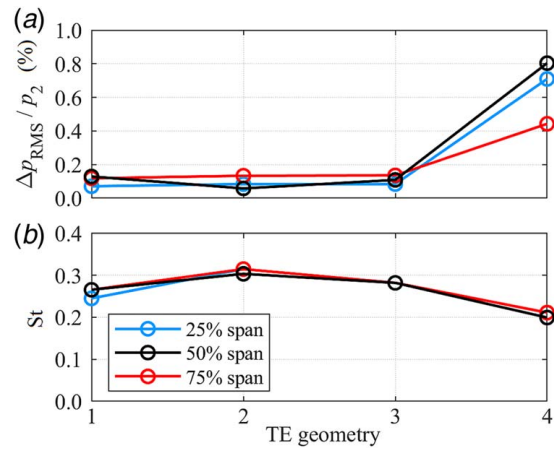

Fig. 4 Wake pressure fluctuations for each of the four geometries at three span locations characterized by: (a) normalized RMS magnitude and (b) Strouhal number

Table 3 Midspan wake pressure fluctuations for each of the four geometries, characterized by normalized RMS magnitude and Strouhal number

Geometry	Overhang length/l	$\Delta p_{RMS}/(p_{01} - \bar{p})$	St
1	1.00	0.13%	0.27
2	0.67	0.06%	0.30
3	0.33	0.11%	0.28
4	0.00	0.80%	0.20

the overhang length becomes short. Figure 5 shows URANS-predicted instantaneous snapshots of the unsteady flow field at midspan for Geometries 1 and 4, focusing on the wake region immediately downstream of the TE. Figures 5(a) and 5(b) show the normalized local KE loss coefficient. The wake region for Geometry 4 is significantly wider than for Geometry 1 and
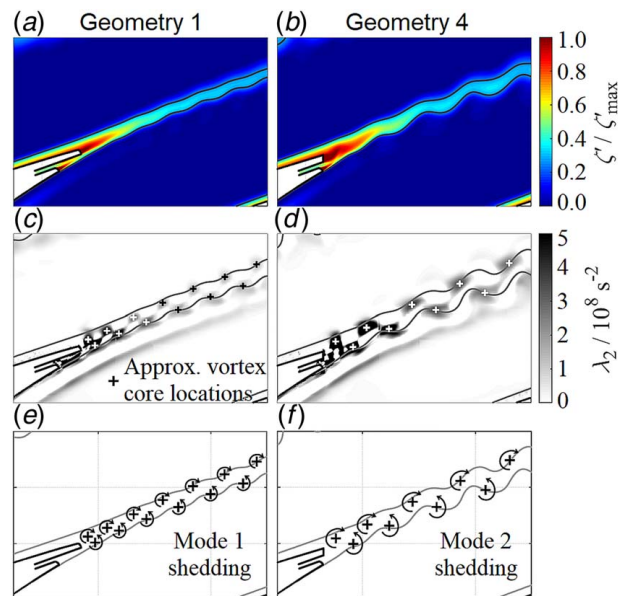

Fig. 5 Midspan URANS CFD snapshots for Geometries 1 and 4 showing: (a) and (b) contours of local KE loss coefficient, ζ', in the wake region; (c) and (d) contours of λ_2 criterion in the wake region; (e) and (f) schematic diagrams of vortex street layouts
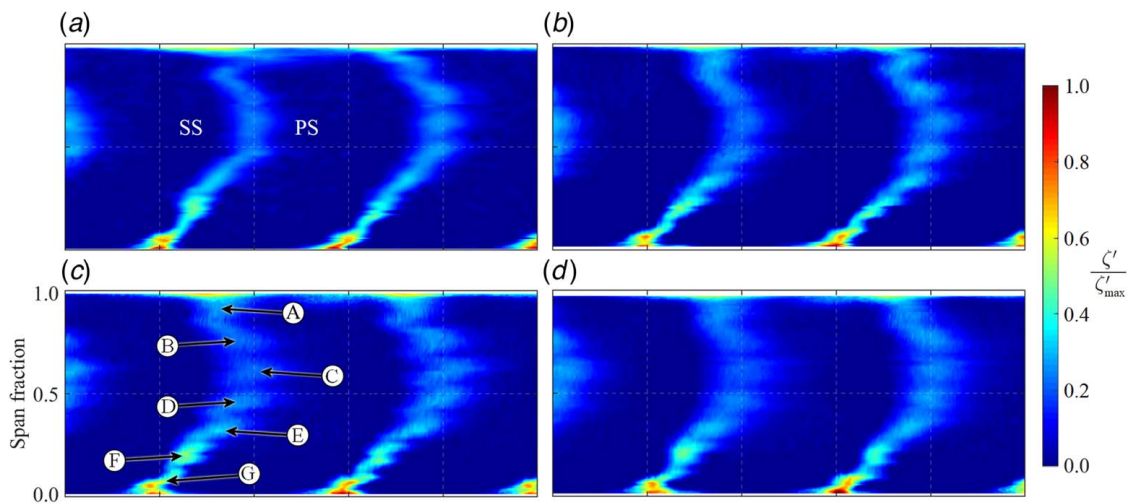
Fig. 6 Experimental distributions of local KE loss coefficient, ζ', in plane 1 ($x/C_x = 0.25$) for each TE geometry: (a) Geometry 1, (b) Geometry 2, (c) Geometry 3, and (d) Geometry 4

has greater unsteady fluctuation from the average position. Figures 5(c) and 5(d) show corresponding plots of the λ_2 criterion to provide an indication of the vortex street arrangement in the wake region. Figures 5(e) and 5(f) show schematic representations of the vortex street structures for Geometries 1 and 4.

We see three key differences moving between Geometries 1 and 4: first, the vortices become more intense (higher λ_2); second, the vortex street becomes wider; and third, the vortices have wider spacing in the streamwise direction, indicating a lower shedding frequency. These observations, which are in line with the pressure fluctuation magnitude and shedding frequency data in Fig. 4 and Table 3, are caused by a change from vortices being shed from the narrow overhanging SS TE land in Geometry 1, to vortices being shed from the entire (SS + PS) base region in Geometry 4 (wider than the SS TE land in Geometry 1 by a factor of 3.2). We refer to these vortex street arrangements as *Mode 1 shedding* and *Mode 2 shedding*, respectively. Shedding from a much wider base region results in the formation of larger eddies at a lower shedding frequency. We return to the idea of Mode 1 and Mode 2 shedding in later sections to explain and understand changes in both the

local distribution and average value of loss coefficient between TE geometries.

Local Loss Coefficient Distributions

Full area surveys of local KE loss coefficient, ζ' (Eq. (2)), measured in experiments in plane 1 are presented in Fig. 6 for all four TE geometries. The data are viewed from downstream to upstream (SS to the left of the wake and PS to the right). URANS CFD data in the same axial plane are presented in Fig. 7.

The wakes have a characteristic bowed shape, reflecting the compound lean of the vanes (see Ref. [20]). The depth of the wake is significantly overpredicted by URANS, and the wake width is underpredicted. The agreement between the experiment and URANS CFD in terms of the absolute loss coefficient is examined in detail in Ref. [20], where it is concluded that approximately 90% of the overprediction of average loss coefficient in the CFD result is caused by overprediction of the total pressure loss associated with film cooling. When comparing local loss coefficient data in an
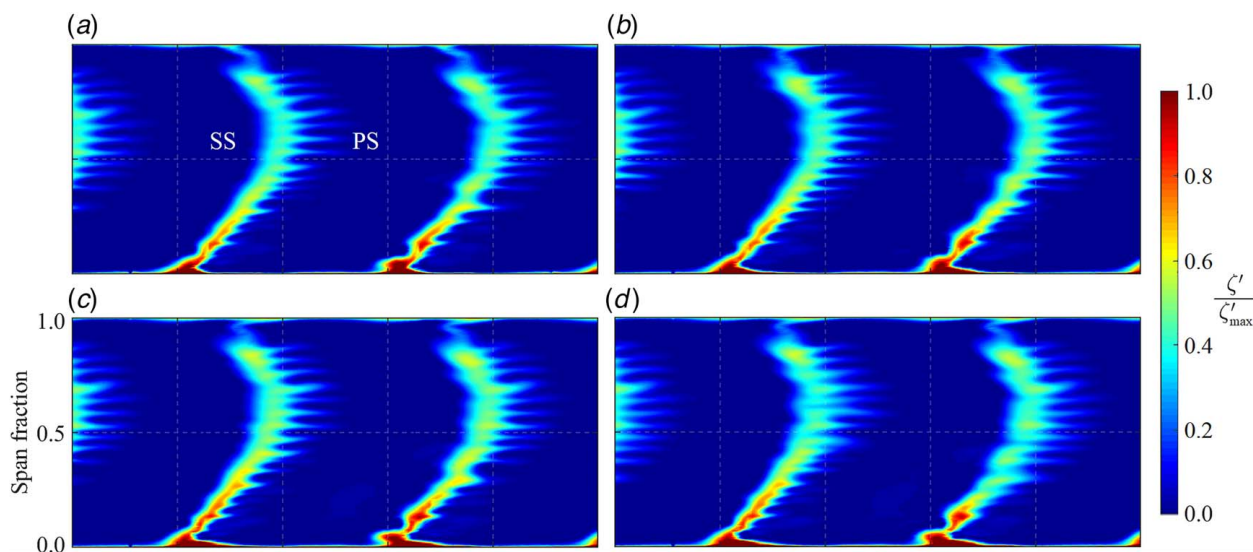

Fig. 7 CFD distributions of local KE loss coefficient, ζ', in plane 1 ($x/C_x = 0.25$) for each TE geometry: (a) Geometry 1, (b) Geometry 2, (c) Geometry 3, and (d) Geometry 4
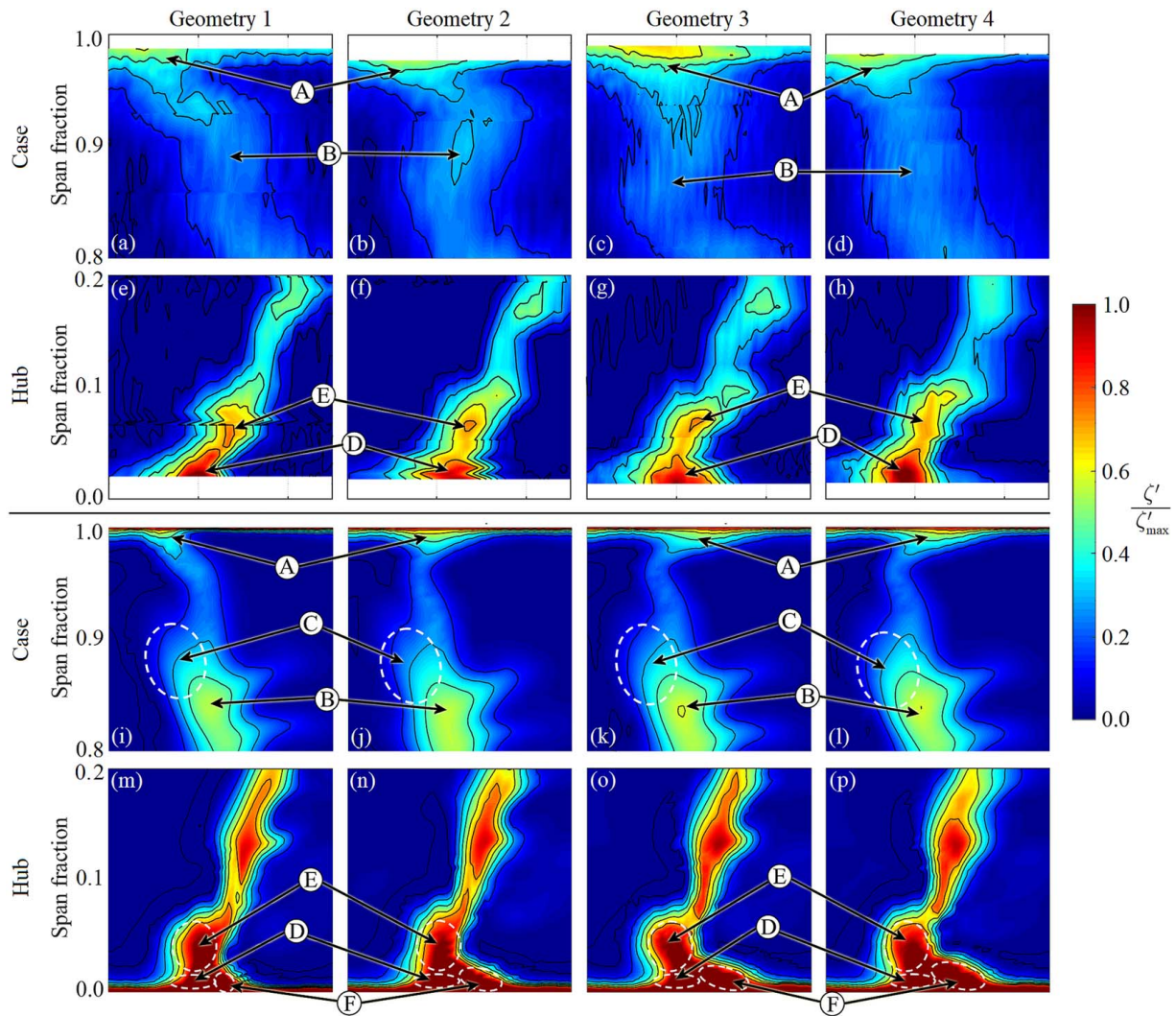
Fig. 8 The wake–endwall junction regions at hub and case for all four TE geometries in (a)–(h) experiment and (i)–(p) CFD

axial plane, the well-known problem in many CFD methods of underpredicting mixing rates also contributes significantly to the disagreement.

In both experiment and CFD, the wake profile has significant radial variation, being deeper and narrower close to the hub. This is caused in part by the lean, sweep and turning profiles of the vane which cause the path length between the local TE and the traverse plane to be lower near the hub (0.64 C_x at 25% span in plane 1) than near the case (0.85 C_x at 75% span in plane 1) (see also Ref. [20]). In the experiment in particular, we also see that the wake is marked by seven discrete peaks in loss coefficient (marked A–G in Fig. 6), separated by local loss coefficient minima. These minima align with the ribs in the internal cooling system. This effect is considered in detail in Ref. [20]. The peaks and minima are much less prominent in the CFD solutions, as they are conflated with horizontal striations to the PS of the wakes. These significantly shorter-scale features can be traced directly to the 17 films on the aft PS row (74% tangential chord). Their high prominence in the downstream flow field is thought to be caused by inadequate modeling of the mixing interaction between the films and the mainstream flow by the source-terms model, and significant underprediction of mixing rates. The high protrusion of these features to the PS of the wakes is exaggerated due to the flow being viewed in axial planes, which cut the wakes at an oblique angle (approximately 75 deg). Notwithstanding these differences in mixing behavior between the CFD and

experiment, we note that otherwise the experiment and CFD are in reasonable agreement.

We now compare the local distributions between the four TE geometries. We make the following observations:

(1) The change in the general shape of the wake signature between geometries is very small. The differences are slightly greater in the experimental data than in CFD.
(2) Wake breadth increases slightly with the decreasing overhang length—an effect that we examine quantitatively in a later section.
(3) In the experiment, the radial non-uniformity of the wakes varies significantly between geometries. The spanwise peaks are more pronounced for Geometries 2 and 3 than for Geometries 1 and 4. This might be explained by the following competing effects: in the covered region upstream of the SS TE, the TE coolant can radially mix, but this effect becomes weaker as overhang length is reduced (shorter covered region) leading to greater radial non-uniformity of the coolant flow as the SS-overhang is progressively shortened; between Geometries 3 and 4, there is a sudden increase in mixing that outweighs the effect of the reduction in covered radial mixing. The latter effect is thought (based on the analysis of local loss coefficient data presented in the later sections) to be caused by the structural shift in the vortex shedding mode (analysis of Fig. 4), although no

unsteady experimental measurements were made to confirm this.

(4) In CFD, the radial non-uniformity changes very little between Geometries 1–3, with only small changes in individual film cooling striations. The Geometry 4 striations are slightly more mixed-out, an effect that is attributed to enhanced mixing due to TE vortex shedding.

(5) The secondary loss cores at hub and case have some sensitivity to TE geometry. We analyze these immediately.

Sensitivity of Secondary Flow Cores to Trailing Edge Geometry. Figure 8 shows close-up views of the wake–endwall junction regions at hub and case for each geometry. The difference in intensity of secondary losses between hub and case is attributed primarily to the downwash effect generated by the radial pressure gradient, which causes low momentum secondary flow to migrate away from the case (case secondary loss cores rapidly disperse) and toward the hub (secondary flow accumulates at the hub and forms intense loss cores). Consider first the case regions shown in Figs. 8(a)–8(d) and 8(i)–8(l). In CFD, the near-wall loss core (marked A) is clearly separated from the wake loss region (marked B) by a region of low loss coefficient (90–97% span). In contrast, in the experimental data, the near-wall loss core and wake loss region are connected. This difference is attributed to an overprediction of the downwash effect of the radial pressure gradient.

The relative circumferential positions of cores A and B move significantly between geometries. In Geometry 1, core A is slightly to the SS (left) of core B. As overhang length reduces, core A gradually extends out to the PS. This change, also seen in CFD, arises because the TE machining operations left a small amount of uncut material at the TE-endwall junction (approximately 2 mm). This is illustrated in Fig. 9. Therefore, as the SS-overhang was progressively shortened, the endwall section and its associated loss core extended further downstream of the SS TE and appear stretched to the right. The extended endwall section is thought to suppress vortex formation from this corner, acting like a splitter plate to disrupt vortex roll-up.

In CFD, the two legs of the hub horseshoe vortex are contained within a single loss region. Dashed circles indicate the locations of the distinct vortices. The PS leg (passage vortex), marked D in frames m–p, is flattened against the hub endwall. The SS leg, marked E in frames m–p, sits just above it (around 4% span) and protrudes to the SS of the wake. These two vortices form a contra-rotating pair with opposing vorticity. The size and the shape of cores D and E varies slightly between geometries, but is not significant to the change in aerodynamic performance.

An additional loss core is located against the hub endwall to the PS of the wake centerline (marked F in frames m–p). Core F corresponds with the blockage of the TE-endwall junction, and a vortex shed from the corner of the TE slot (equivalent to core A at the case). Core F grows as overhang length is reduced, extending further out to the PS of the wake. Again, this change results from vestigial overhang material at the TE-endwall corner (same cause as the shift in core A).
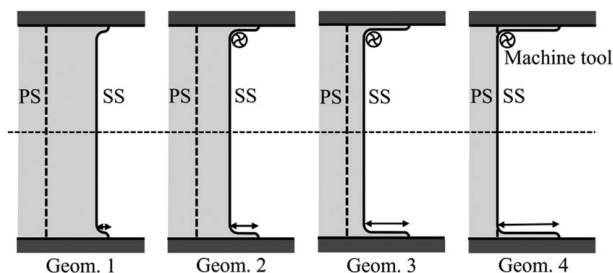
Radial Profiles of Kinetic Energy Loss Coefficient and Whirl Angle. In Fig. 10, we present radial profiles of circumferentially mass-flux-averaged KE loss coefficient, $\zeta''(r)$ (Eq. (3)), for each TE geometry in plane 2. These data are analyzed further downstream of the TE than that in Figs. 6 and 7 (0.50 C_x as opposed to 0.25 C_x), to reduce the degree to which radial non-uniformity obscures other changes between geometries. Comparisons between planes are omitted for brevity.

We first observe that there is a large region of relatively constant loss coefficient, which extends between 20–85% span in experiment and between 10–80% span in CFD. We refer to this as the *profile loss region* because in this region, the flow is relatively 2D and unaffected by secondary flow. Outside the profile loss region, the loss coefficient grows rapidly due to a combination of secondary flow and accumulation of endwall boundary layer fluid. In the CFD solutions, there is a very pronounced loss coefficient minimum just outside the case boundary layer. This arises because of an overprediction of the downwash effect, resulting from undermixing of the low momentum case boundary layer fluid.

In the experimental data, we measure a clear rise in the average loss coefficient as we move progressively from Geometry 1–4. We see the same increase in the CFD data, but the magnitudes of the changes are smaller, and the effect is less visually obvious due to greater radial variation in the loss coefficient profile. Considering the profile loss region, between Geometries 1 and 4, ζ'' rose by an average of +27.3% in experiment and by +11.8% in CFD. The percentage increases for each geometry change are summarized in Table 4.

The experimental data show a moderate rise in ζ'' between Geometries 1 and 2, a large rise between Geometries 2 and 3, and a relatively small rise between Geometries 3 and 4. In CFD, there were roughly equal, moderate increases for the geometry changes 1–2 and 2–3, and only a very small increase for the geometry change 3–4. The mechanisms explaining these trends are explored later in this article.

We now quantify the radial non-uniformity in the profiles by comparing the RMS amplitude of fluctuations over the profile loss region. These are tabulated in Table 5, expressed as a percentage of ζ'. In all cases, the magnitude of fluctuations is greater in CFD than in experiment (average of 11.68% across all geometries, compared to 8.21% for experiment) due to the undermixed individual films (striations in Fig. 7). In CFD, the amplitude of radial fluctuations first rises between Geometries 1 and 3, but then falls between Geometries 3 and 4. This fall in magnitude reflects the enhanced mixing rate close to the TE, caused by the increased
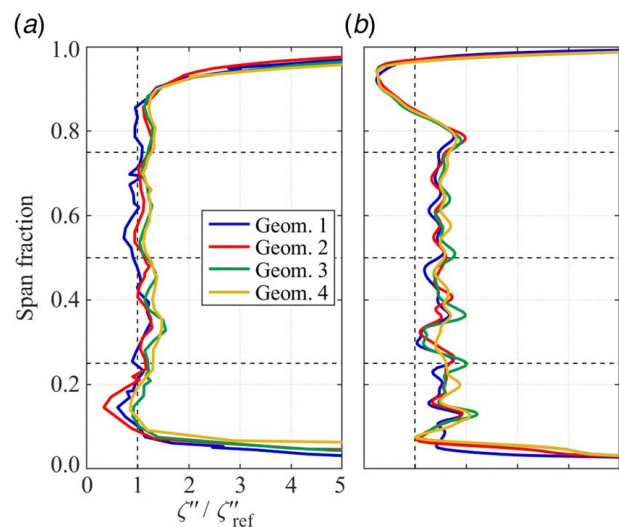

Fig. 9 Schematic diagram of TE machining phases illustrating residual TE overhang material at the TE-endwall corner

Fig. 10 Radial profiles of circumferentially mass-flux-averaged KE loss coefficient, $\zeta''(r)$, in plane 2: (a) experiment and (b) CFD

Table 4 Percentage changes in average loss coefficient (ζ'') in the profile loss region for plane 2

	% change in average ζ'' with respect to geom. 1	
Geometry change	Experiment	CFD
1–2	+8.59	+5.79
1–3	+24.49	+10.39
1–4	+27.27	+11.75

Table 5 RMS amplitudes of radial fluctuations in ζ'', in plane 2

	$\Delta\zeta''_{RMS}/\zeta''_{mean}$ (%)	
Geometry	Experiment	CFD
1	8.30%	11.21%
2	9.71%	11.67%
3	8.75%	14.06%
4	6.09%	9.78%

magnitude of TE vortex shedding and the structural change from Mode 1 to Mode 2 shedding. In the experimental data, we see the same effect, but the amplitude starts to fall between Geometries 2 and 3. This result suggests that the structural change in TE vortex shedding occurs at longer SS-overhang length in the experiment than in the CFD (noting that unsteady experimental evidence was not available). We return to this idea in later sections.

The corresponding radial profiles of circumferentially mass-flux-averaged turning (or whirl) angle, β, in plane 2 are plotted in Fig. 11. β is defined as the angle between the local flow direction and the axial direction in an axial-circumferential plane. Higher values of β therefore indicate flow further from axial (higher turning). The experimental profiles extend close to the hub and case endwalls, but the small regions of missing data result from the finite size of the five-hole probe.

The radial profile shape was very well matched between experiment and CFD. The mean whirl angle steadily increases from 17 to 66% span and is approximately constant from 66 to 93% span. The difference in the mean whirl angle between experiment and CFD, averaged over the profile loss region (same radial ranges as in
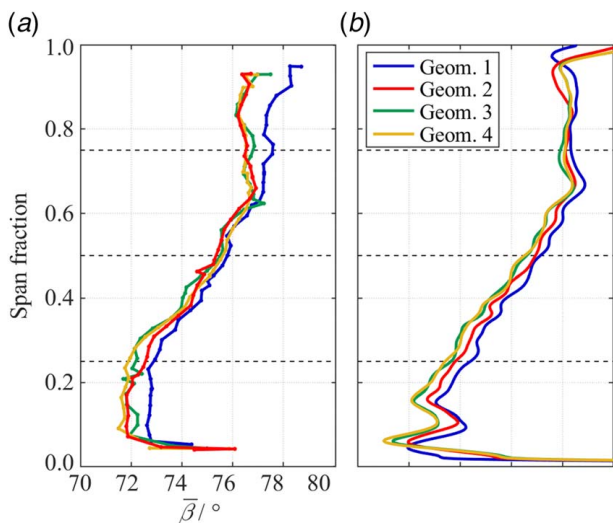

Fig. 11 Radial profiles of circumferentially mass-flux-averaged whirl angle, β, in plane 2: (a) experiment and (b)

Fig. 10) and across all four TE geometries, was 0.84 deg. This is a small absolute offset, showing good capability in this prediction, and is of the same order of magnitude as the estimated overall bias error of the probe (combined uncertainties associated with ECAT measurements and in the probe calibration process).

The radial profile of the whirl angle is largely unchanged with TE geometry. There is a small reduction in the mean whirl angle in the profile loss region as overhang length reduces. The offsets in $\bar{\beta}$ (averaged over the profile loss region) for each of Geometries 2–4 with respect to Geometry 1 are tabulated in Table 6.

In the experiment, the reduction in the mean whirl angle with respect to Geometry 1 is almost the same for Geometries 2–4. That is, the changes among Geometries 2–4 are insignificant. CFD and experiment are in reasonable agreement, but there is a further significant reduction in the mean whirl angle between Geometry 2 and 3 in the CFD predictions, which was not recorded in the experiment. The small reduction in the whirl angle is attributed to a reduction in the guided length offered by the TE overhang as the overhang length is reduced. Once the overhang is sufficiently short (at Geometry 2 in the experiment and Geometry 3 in the CFD), further reduction appears to cause negligible change in the mean whirl angle: this would be expected in a largely separated base region. The difference between CFD and experiment is most likely caused by differences in the unsteady interaction, mixing and shedding of the mainstream and TE flows around the TE slot exit.

Outside of the profile loss region the CFD profiles show regions of overturned secondary flows just outside of the hub boundary layer. In the experimental data, these overturned regions are more fully mixed out. The experimental data also show a notably higher mean whirl angle for Geometry 1 outside of the profile loss region (below 20% span and above 70% span) than the other geometries. This is likely caused by deviations of the hand-dressed SS-overhang from the nominal CAD geometry. The effect is not present for Geometries 2–4, which have a sharp-edged termination of the TE. The differences in the whirl angle between the TE geometries were approximately the same outside the profile loss region as within it.

Analysis of Wake Circumferential Profiles

In this section, we consider the impact of TE geometry on circumferential profiles of local loss coefficient and whirl angle at a number of radial heights. Figure 12 presents circumferential profiles of the local KE loss coefficient, ζ' (Eq. (2)), over a single wake period at three spanwise locations in plane 1. Each profile is radially averaged over ±5% of span to reduce sensitivity to small radial non-uniformities—in the experimental data, this corresponds to four sweeps of the traverse probe.

All of the profiles (Fig. 12(a)–12(f)) have a quasi-normal distribution with slight asymmetry, such that the decay in loss coefficient from the peak is steeper on the SS than on the PS. This is not a simple function of accumulated deficit: the SS boundary layer momentum thickness just upstream of the TE separation point is approximately 20 times larger than that on the PS (based on boundary layer profiles at the TE predicted by fully cooled URANS simulations; note that the extremely large ratio is at the extreme SS TE

Table 6 Changes in circumferentially averaged whirl angle in plane 2 averaged over the (radial extent of) profile loss region

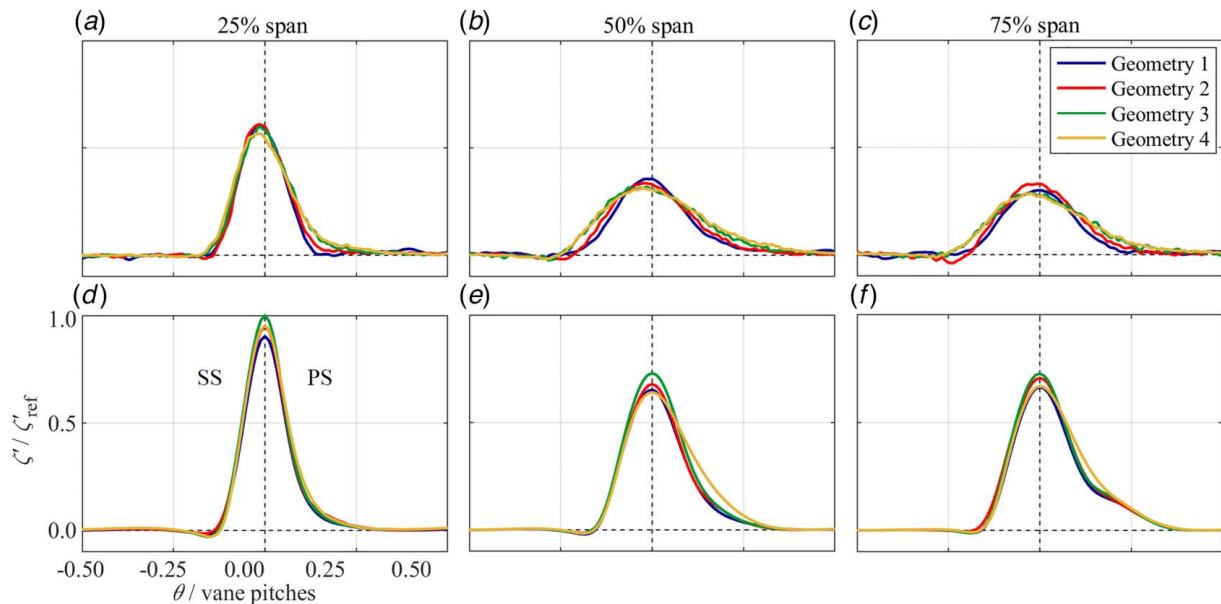|	Change in $\bar{\beta}$ with respect to Geometry 1	
Geometry change	Experiment	CFD
1–2	−0.45 deg	−0.32 deg
1–3	−0.48 deg	−0.65 deg
1–4	−0.47 deg	−0.64 deg

Fig. 12 Circumferential profiles of local loss coefficient, ζ', compared between the four TE geometries at 25%, 50%, and 75% span in plane 1: (a)–(c) experiment and (d)–(f) URANS CFD

downstream of a shock-impingement region). This analysis is described in more detail in Ref. [25]. Indeed, the overall deficit in the wake is dominated by the separation loss (or *pressure drag*), with the integrated boundary layer loss accounting for only approximately 45% of the overall loss in the profile region. Thus, such a result should not be necessarily surprising. A further contributing effect worth noting is that the streamwise path length between the PS TE lip a given traverse plane (e.g., plane 1) is greater than the equivalent dimension for the SS TE lip—by as much as 0.14 C_x for Geometry 1, dropping to 0.02 C_x for Geometry 4. The effect arises because (as is convention) we traverse in an axial plane, as opposed to a streamwise-normal plane. We see later in the context of analyzing the wake width as a function of axial distance that this could account for approximately 45% of the observed asymmetry in the wake profile (when the SS-overhang is relatively long, and the traverse plane is relatively close to the TE, e.g., plane 1).
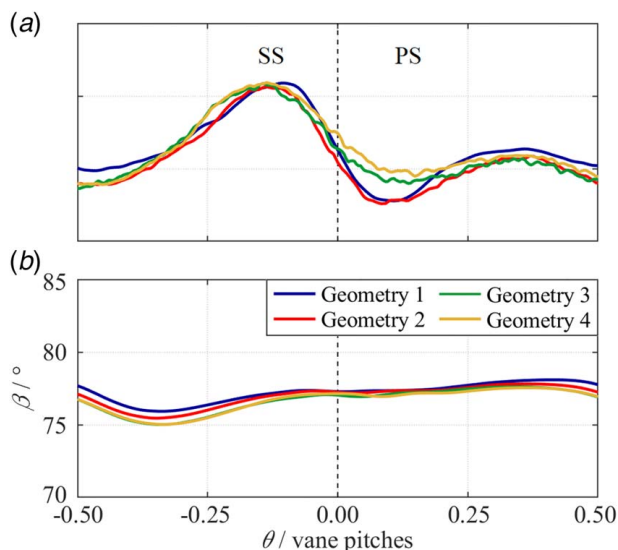

Fig. 13 Circumferential profiles of whirl angle at midspan in plane 1 from: (a) experiment and (b) URANS CFD

Continuing this theme, the differences in peak height and width between the three spanwise locations are driven largely by radial variations in vane lean, sweep, and whirl angle, which cause differences in the streamwise path length between the TE and the traverse plane. This is an interesting effect that has been analyzed in detail in Ref. [20], and the analysis will not be repeated here. It was shown that if the data are presented (unconventionally) in terms of *streamwise path length from the TE*, a good collapse of the wake width trends at different radial heights can be achieved.

An interesting secondary feature in the CFD data of Fig. 12(f) is the weak secondary peak between $0.15 < \theta < 0.25$, caused by partially mixed late-PS films. This was discussed in the context of Fig. 7.

Consider now the differences in wake profile shape between the four TE geometries. The CFD profiles in Fig. 12(d)–12(f) show almost identical profile shapes between Geometries 1 and 3 at all three spanwise locations, differing only in the peak height. The peak height rises on average (of three spanwise locations) by +5.16% between Geometries 1 and 2 and by +5.19% between Geometries 2 and 3. Geometry 4 differs from the general trend in two ways: first, the peak height falls relative to Geometry 3; and second, the PS of the wake profile broadens at 50% and 75% span. These effects are attributed to enhanced mixing close to the TE, due to stronger vortex shedding (Mode 2 shedding) in Geometry 4 (Fig. 4). At 25% span, the effect is much weaker because the streamwise path distance between the TE and plane 1 is significantly shorter, and thus, the additional mixing has less path length in which to cause an effect.

Looking at the experimental profiles shown in Figs. 12(a)–12(c), we see two distinct pairs: Geometries 3 and 4 have a lower peak height (by an average of −8.1%), and a greater width, than Geometries 1 and 2, for all three spanwise locations. Again, the difference is smaller at 25% span. The suggestion is that the apparent additional mixing seen in Geometry 4 in URANS CFD (evidence of reduced radial non-uniformity in Table 5 and lower and broader peak in Fig. 12) is present for *both* Geometries 3 and 4 in the experimental data. That is, as mentioned previously, the structural change from Mode 1 to Mode 2 shedding occurs at longer SS-overhang length in the experiment than in the CFD.

Midspan circumferential profiles of whirl angle in plane 1 are plotted in Fig. 13. The difference in profile shapes between experiment and URANS CFD is immediately noticeable. Experimental

profiles show the expected transition across the wake center from a maximum on the SS to a minimum on the PS, corresponding with the difference in exit metal angle. In contrast, the URANS simulations predict very little circumferential variation in the whirl angle across the wake. This is attributed to an overprediction of shock–boundary layer interaction on the late SS, causing early separation. The effect is discussed in more detail in Ref. [20].

Comparing the midspan whirl angle distributions between TE geometries, we see two main differences. First, there are small offsets in the local whirl angle in the freestream away from the wake ($\theta < -0.25$ and $\theta > 0.40$), in agreement with the offsets in average whirl angle in the profile loss region (Fig. 11 and associated analysis). This effect is caused by the changes in covered turning of the vane as the SS-overhang is progressively shortened.

Second, in the experimental data, there is a notable increase in the minimum whirl angle just to the PS of the wake ($0.0 < \theta < 0.2$) between Geometries 2 and 3. The difference between the SS peak and PS trough drops from an average of 8.1 deg for Geometries 1 and 2 to an average of 6.7 deg for Geometries 3 and 4. This is thought to be due to a change to more aggressive and larger length scale (Mode 2) mixing, which enhances the low near-PS whirl angles by averaging over larger length scales in the TE region.

Analysis of Wake Mixing Rate

In this section, we examine the change in the wake mixing rate with TE overhang length. We characterize the circumferential profiles of local loss coefficient (Fig. 12) using a peak local loss coefficient, $\widehat{\zeta'}$, and a wake width, w. Here, the width is defined as the fraction of vane pitch over which the local loss coefficient exceeds 50% of the peak value. These two parameters are plotted in Figs. 14 and 15, respectively, as functions of *true axial distance* from the TE normalized by axial chord length, x'/C_x, using data from the midspan section. The true axial distance is the distance measured from the midspan TE extent *for each geometry*. This distinction corrects for the small changes in the axial location of the SS TE tip between geometries as the SS-overhang is progressively shortened. Notwithstanding small differences in the whirl angle at midspan (see Fig. 11), x' can be taken as a proxy for the true streamwise distance between the TE and the measurement plane. The purpose of this clarification is to distinguish the differences in wake shape *due to changes in TE geometry*, from differences that arise due to changes in distance between the TE and the traverse plane. It has been demonstrated in the previous work [20] that apparently dissimilar wake profiles can be collapsed to a large extent when moving from an absolute axial co-ordinate system to a local streamwise co-ordinate system. In the current case, we
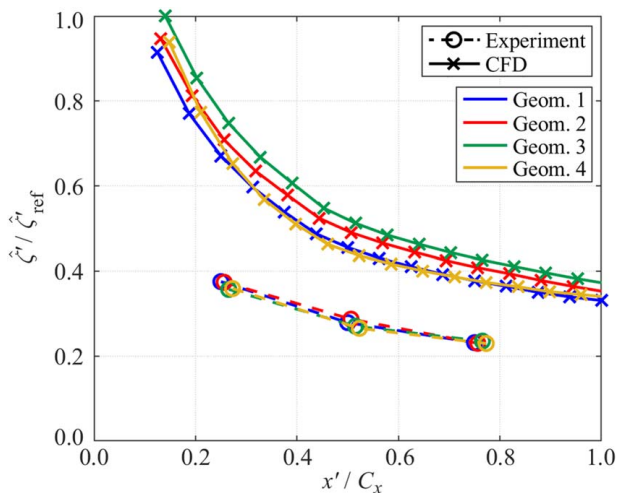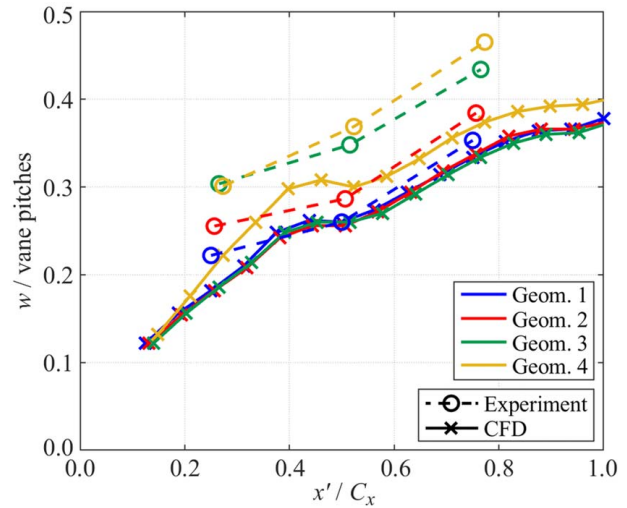

Fig. 15 Wake width, _w_, at midspan as a function of true axial distance

demonstrate that this is not a significant factor, because the predominant effects arise due to TE design changes.

Consider first the peak loss coefficient data of Fig. 14. The peak loss coefficient values for both experimental and CFD data follow a quasi-exponential decay with x'/C_x. The shape of the decay characteristics is considered in detail in Ref. [20].

Absolute values of peak loss coefficient in a particular axial plane follow the trends observed in Fig. 12: in CFD, $\widehat{\zeta'}$ rises moving from Geometry 1 to Geometry 3 and falls for Geometry 4; in the experiment, $\widehat{\zeta'}$ is higher for Geometries 1 and 2 than Geometries 3 and 4, but the differences between geometries are much smaller than in the CFD predictions. The experimental values of the peak loss coefficient are approximately half those for CFD due to undermixing in the CFD solution. For the CFD data, the shape of the trends is almost identical for Geometries 1–3, but Geometry 4 has a steeper rate of decay close to the TE and a shallower gradient further downstream. This is caused by stronger vortex shedding close to the TE. The same pattern is true in the experimental data, but with steeper initial decay for both Geometries 3 and 4. This supports the hypothesis of a shift to Mode 2 vortex shedding for both Geometries 3 and 4 in the experiment, promoting mixing close to the TE. For completeness, we note (by inspection of the trends) that the impact on the differences between trends of moving from absolute to *true* axial distance is small in comparison to the differences due to TE design.

We now consider the trend of wake width with x'/C_x in Fig. 15. Looking first at the experimental data, we see an approximately linear increase in the wake width with axial distance (as the wakes mix out) and an increase in width as the overhang length is reduced. The differences in wake width between geometries are significantly larger in the experiment than in the CFD data, in line with the observations of Fig. 12. There is a distinct separation between the trends for Geometries 1 and 2 and those for Geometries 3 and 4, supporting the structural change in the vortex shedding.

The CFD data, analyzed at finer axial resolution, show a more complex trend with local plateaus at $x'/C_x = 0.50$ and 0.90. These modulations in the gradient of the wake width arise as the wakes pass through periodic streamwise pressure gradients—this is analyzed in more detail in Ref. [20]. We note that while the experimental data are relatively sparse, the data are consistent with a similar plateau at approximately $x'/C_x = 0.50$. There is a significant difference between Geometry 4 and all other geometries, both in terms of the initial rate of increase of wake thickness (in the range $0.00 < x'/C_x < 0.40$) and the absolute thickness at every axial station. This supports the argument for a shift from Mode 1 to Mode 2 shedding between Geometries 3 and 4 in the CFD.
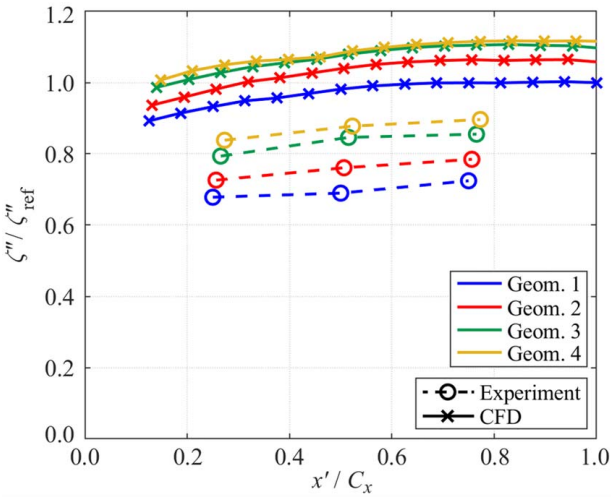

Fig. 14 Peak KE loss coefficient, $\widehat{\zeta'}$, at midspan as a function of true axial distance

Fig. 16 Circumferentially mass-flux-averaged KE loss coefficient, ζ'', at midspan as a function of true axial distance

In Fig. 16, we present midspan trends with true axial distance of circumferentially mass-flow-averaged KE loss coefficient, ζ'' (Eq. (3)). Both experiment and CFD show an increase in the average loss coefficient moving axially downstream as remaining secondary kinetic energy (SKE) is mixed out and becomes manifest as loss. The URANS simulations overpredict average loss coefficient by an average of 32.1% (across all geometries and axial stations). The axial gradient of average loss coefficient is very similar among the four TE geometries and between CFD and experiment. As the overhang length is progressively reduced, the average loss coefficient in a given axial plane increases. We analyze this effect in more detail in the following section.

The primary conclusion is that TE overhang length has only a very small impact on the wake mixing rate. In cases where Mode 2 shedding occurs, mixing is biased toward the TE, leading to higher rates of peak local loss coefficient decay, and of wake thickening, near the TE. Shorter TE overhangs have a higher average loss coefficient, but the effect must be separated from changes in the SS TE thickness.

Analysis of Overall Aerodynamic Performance

We now assess the overall change in aerodynamic performance between the four TE geometries, by comparing plane-averaged and mixed-out average KE loss coefficients for the profile loss region. We consider only this region, so as to isolate the effect of the change in TE design, having already shown (Fig. 8 and the associated analysis) that secondary losses do not change significantly with overhang length, being primarily a function of the detailed TE-endwall junction geometry.

Plane-average KE loss coefficients, ζ''' (Eq. (4)), and mixed-out average KE loss coefficients, ζ'''' (Eq. (5)), are presented in Fig. 17. Data are obtained from plane 3 to reduce the sensitivity to local gradients (flow more mixed out) and to reduce the sensitivity to inaccurate estimation of the SKE (lower absolute value due to partial mixing out by this plane). The profile loss region, over which the average was taken, was between 20% and 80% span. The experimental and CFD data are each normalized with respect to their *respective mixed-out* average loss coefficient for Geometry 1, ζ_1''''. The mixed-out average loss coefficient was calculated using the method of Dzung [24], which is discussed in detail in the context of the current experiment in Refs. [20,23].

It is worth briefly expanding on the two choices implied by the chosen normalization method. The reason the *respective* condition was chosen is to highlight the changes in aerodynamics with TE design, as opposed to focusing on the absolute accuracy of the
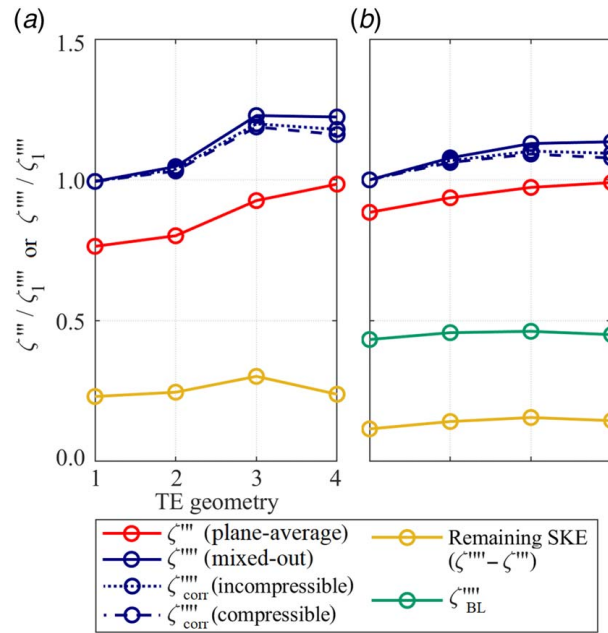

Fig. 17 Plane-average and mixed-out average KE loss coefficients in the profile loss region, normalized with respect to ζ_1'''' (data from plane 3): (a) experiment and (b) CFD

CFD method: it has been shown earlier and by more comprehensive analysis in Ref. [20] that the URANS simulations overpredict absolute mixed-out average KE loss coefficient by approximately 4.0%. The *mixed-out* condition was chosen (for a detailed discussion of the choice of methods, see Ref. [23]) because it gives the best representation of overall loss generation by the vane (i.e., both loss already manifest, and inevitable additional loss due to mixing out of SKE) and removes the sensitivity in the comparison to SKE at a particular plane. This is particularly important because of the well-known tendency of URANS to underpredict the mixing rate.

First, we consider the plane-averaged and mixed-out average values of loss coefficient. The difference between these is the *residual SKE* (or remaining SKE). This is an estimate of the unavoidable additional mixing loss downstream of plane 3. The residual SKE in the experiments is approximately double that predicted by URANS. This is attributed to the greater circumferential variation in whirl angle in the experiment (Fig. 13), which provides an additional mechanism for generating mixing loss [23].

The trends in both experiment and CFD are for increasing mixed-out average KE loss coefficient as the SS-overhang is progressively shortened. We now attempt to separate the effect due to aerodynamics from that due to TE overhang thickness (t_{SS}, see Fig. 2). We do this by scaling the mixed-out average KE loss coefficients for each geometry in knowledge of the SS TE thickness. The scale factors were calculated using an adaptation of the control volume-based method first described by Stewart [27] and developed by Deckers and Denton [28]. The adapted model is described in the Appendix, and the resultant scale factors for each of Geometries 2–4 are summarized in Table 7. Scale factors for both compressible and incompressible conditions are presented for completeness, but we focus on the compressible condition.

Table 7 Scale factors for each of Geometries 2 to 4

Geometry	2	3	4
ζ'''' scale factor (incompressible)	0.991	0.976	0.964
ζ'''' scale factor (compressible)	0.985	0.967	0.949

The compressible scale factors imply reductions in the mixed-out KE loss coefficient to account for variation in the SS TE thickness of 1.5%, 3.3%, and 5.1% for geometry changes 1–2, 1–3, and 1–4, respectively. These can be compared with the thickness changes in Table 2, but it is worth nothing that the SS TE land is only one of the several low base pressure regions in the control volume method. Applying the compressible correction factors to the data of Fig. 17 results in the *corrected* mixed-out average profile loss coefficient (ζ''''_{corr}) and modifies the trend of mixed-out average loss coefficient to the dotted (incompressible) and dashed (compressible) lines. This is the best estimate of the mixed-out loss coefficient scaled to a common SS TE thickness ($t_{SS,1}$). This correction changes the trend from a monotonic increase to a slight drop in mixed-out average loss coefficient between Geometries 3 and 4.

For completeness, percentage changes in both plane-average and *corrected* mixed-out average profile loss coefficient for each geometry change are presented in Table 8. The experimental and CFD percentage changes are referenced to their *respective mixed-out average loss coefficient for Geometry 1*, ζ''''_1. The remainder of the analysis focusses on corrected mixed-out average profile KE loss coefficients.

The experimental data show a small rise in corrected mixed-out average KE loss coefficient between Geometries 1 and 2 (+3.8%), a large rise between Geometries 2 and 3 (+15.6%), and a small *decrease* between Geometries 3 and 4 (−2.7%). The gross trend in the CFD was similar to the experiment, but with corresponding changes +6.2%, +3.0%, and −1.5%. That is, changes of approximately half the magnitude, and with a much smaller change in corrected mixed-out average loss coefficient between Geometries 2 and 3 than in the experiment. In the next section, we try to understand these changes.

Boundary Layer Loss, Base Pressure, and Vortex Shedding Mechanisms

In this section, we consider the contributions of boundary layer loss, base pressure loss, and vortex shedding mechanisms to the overall corrected mixed-out average KE loss coefficient, in an attempt to reconcile the observed changes between geometries (Table 8). We first consider the boundary layer loss.

Boundary Layer Loss. The green line in Fig. 17(*b*) shows the estimated KE loss coefficient associated only with the surface boundary layers for each TE geometry in the CFD. We refer to this as ζ''''_{BL}. These data were calculated from the SS and PS boundary layer velocity profiles at the TE at midspan (we assume that the boundary layer profiles are sufficiently radially uniform over the profile loss region for our present purpose), using the method described in Ref. [29]. Boundary layer profiles for the same data set are presented in Ref. [25]. The changes in the KE loss coefficient associated with boundary layers were +0.0%, +1.3%, and −0.4% of ζ''''_1 for the geometry changes 1–2, 1–3, and 1–4, respectively. These contributions are summarized in the last column of Table 8. These very small changes in loss coefficient (with respect to Geometry 1) are primarily caused by small differences

in the SS boundary layer thickness, driven by changes in shock–boundary layer interaction on the mid-to-late SS.

Comparing the changes in the KE loss coefficient associated with boundary layers with the overall URANS-predicted changes in *corrected* mixed-out average KE loss coefficient (Table 8), we see that on average (across the three geometry changes), ζ''''_{BL} accounts for only 3.5% of the change in ζ''''_{corr}.

We conclude that while the changes in SS shock–boundary layer interaction do contribute to the change in ζ''''_{corr}, they are almost insignificant in the overall result. In the following subsections, we consider changes in base pressure loss and in vortex shedding behavior.

Base Pressure Drag. We now consider the contribution of base pressure loss to overall corrected mixed-out average profile KE loss coefficient. Note that the analysis in this section is based on base pressure data from the CFD study only—no experimental base pressure measurements were made.

Figure 18 compares normalized pressure distributions over the SS and PS TE bases at midspan for each TE geometry, from the URANS CFD simulations. The abscissa represents distance normal to the TE slot exit direction, with the origin at the slot centerline. The left- and right-hand sides of the figure show the pressure distributions around the SS and PS bases, respectively. Base pressure distributions were compared between different radial locations (not shown), and while the absolute pressures varied in line with the radial pressure gradient (higher pressures close to the case), the shape of the distributions and the changes with TE geometry varied little with span. We therefore consider the change with span unimportant and analyze midspan data only.

On the PS, mainstream flow expands around the PS TE corner and then separates from the TE. The expansion results in the sharp dip at $y/t_s \approx 1.5$. The pressure then settles to an approximately constant value over the PS *base region* (marked by vertical dashed lines). Another expansion can be seen at the inner corner of the PS base region, where the TE coolant flow expands slightly around the inside TE corner. In the approach to the SS TE corner, the mainstream flow is diffused slightly (approaching the mean TE pressure, and consistent with a small deviation angle *towards* axial) before settling to an approximately constant value in the SS base region. There is a sharp diffusion at the SS inner corner where flow expands around the TE inner corner.

Table 8 Changes in plane-average, corrected mixed-out average, and boundary layer KE loss coefficients for the profile loss region with respect to Geometry 1 (data from plane 3)

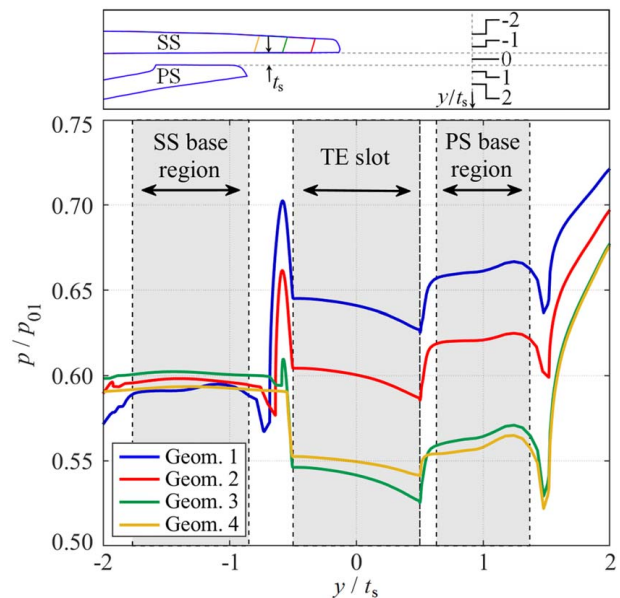| Geometry change	Experiment		CFD		
	ζ'''	ζ''''_{corr}	ζ'''	ζ''''_{corr}	ζ''''_{BL}
1–2	+3.8%	+3.8%	+5.2%	+6.2%	+0.0%
1–3	+16.3%	+19.4%	+8.9%	+9.2%	+1.3%
1–4	+22.1%	+16.7%	+10.6%	+7.7%	−0.4%

Fig. 18 Midspan base pressure distributions

We now compare PS and SS base region pressure distributions for each of the four geometries. The SS base region pressure distributions are almost flat and change relatively little between geometries (very slight increase in pressure between Geometries 1 and 3, then a small drop in pressure to Geometry 4). The PS base region pressure distributions are also relatively flat, but, in contrast to the SS base region distribution, have large falls in pressure between Geometries 1–3, but little further drop between Geometries 3 and 4. All four geometries have significant differences in pressure between the SS and PS base regions.

Average SS and PS base region pressures ($\overline{p_b}$) for each geometry were calculated by taking the mean over the regions of approximately constant pressure indicated by the shaded regions in Fig. 18. The average values are plotted in Fig. 19, as both fractions of inlet total pressure, $\overline{p_b}/p_{01}$ (Fig. 19(a)), and as base pressure coefficients, C_{pb} (Fig. 19(b)), defined by

$$C_{pb} = \frac{\overline{p_b} - \overline{p_2}}{p_{01} - \overline{p_2}} \qquad (6)$$

where $\overline{p_2}$ is the circumferentially-averaged static pressure at the cascade exit plane. Although this is a conventional definition of base pressure coefficient, we note that the choice of reference pressure (i.e., $\overline{p_2}$) is arbitrary because of the separation between the TE location and the nominal cascade exit plane, and also the significant static pressure variation across the passage (see analysis in Ref. [19]). Notwithstanding this point, the base pressure coefficient is taken to provide a more useful expression of base pressure drag than $\overline{p_b}/p_{01}$, because it is normalized with respect to the dynamic head of the freestream flow.

The trends of $\overline{p_b}/p_{01}$ (Fig. 19(a)) are in accord with the observations of Fig. 18: the SS base pressures are relatively insensitive to overhang length (maximum difference between any two geometries of 0.9% of p_{01}), but the PS base pressures fall sharply between Geometries 1 and 3 as overhang length is progressively reduced. An explanation for the change in base pressure trends is given in Ref. [25]. The relevant points are now briefly summarized.

As overhang length is reduced between Geometry 1 and 3, the downstream region of low static pressure (associated with the uncovered turning of the vane) extends further upstream, into the vane passage. This is the result of a change in overall vane aerodynamics around the *controlling region* of the vane passage. Here, by controlling region, we mean the region around unit Mach number, to which we traditionally ascribe the term *throat* in a 1D framework. This is discussed in detail in Ref. [25].
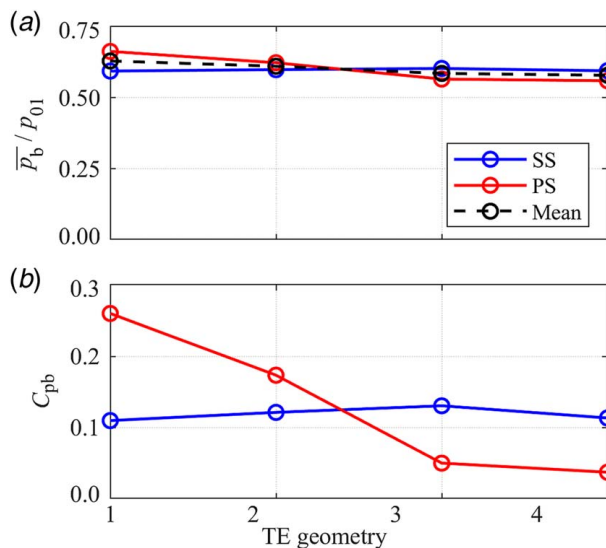
As the low static pressure region migrates upstream, it affects the base region pressure. As the SS-overhang is progressively shortened, the location of the SS TE moves upstream (see Fig. 2). For the particular geometry studied, this displacement is similar in magnitude to the displacement of the static pressure contours, and therefore, SS TE base region pressure has low sensitivity to overhang length. In contrast, the location of the PS TE remains fixed as the SS-overhang is shortened (see Fig. 2), so the PS TE base region pressure has higher sensitivity to upstream migration of the low static pressure region.

We now briefly consider base pressure coefficient trends in Fig. 19(b). The C_{pb} trends are (of course) broadly similar to those for $\overline{p_b}/p_{01}$. We note that the coefficient values are everywhere positive. This is due to uncovered turning, which occurs between the SS and PS base regions and the cascade exit plane, which is located a short distance downstream of the TE.

We conclude by noting that, in the literature, a close association between base region pressure and overall (mixed-out average) loss has been drawn. This is natural because low base region pressure should intuitively be associated with higher *pressure drag* on a component. However, in an attempt to correlate the two, we have noted that, for our geometries, the change in base region pressure is associated with a change in overall vane aerodynamics at the same nominal operating point (based on the pressure ratio). This latter effect is significant and means that the base region pressure change cannot be analyzed in isolation. That is, correlations between loss coefficient and base region pressure may have little meaning without a more holistic analysis of the vane pressure field. We feel this is a topic that merits more detailed analysis.

Vortex Shedding Mode and Transonic Vortex Shedding. In this section, we briefly review an apparent discrepancy between the CFD and experimental results in terms of corrected mixed-out average loss coefficient, which we believe may arise because of the inability of the URANS CFD method to accurately predict a transonic vortex shedding effect.

Accepting corrected mixed-out average KE loss coefficient as the best measure of overall loss, we recall that the increase in corrected mixed-out average loss coefficient between Geometry 2 and 3 was much larger in the experiment than in CFD. This was discussed in the context of Fig. 17 and Table 8.

The wake width data (Fig. 15) provide clear evidence of an enhancement of near-TE mixing between Geometry 2 and 3 in the experiment and between Geometry 3 and 4 in the CFD. We suggest that this effect is associated with a structural change between Mode 1 and Mode 2 vortex shedding. Direct analysis of vortex sheet patterns (Fig. 5) and indirect evidence from the Strouhal number changes (Table 3) confirm that that such a mode change occurs between Geometry 3 and 4 in the CFD. It is tempting to assume that the change in the shedding mode should be related to a significant rise in loss coefficient. Such an assumption would be compatible with the experimental data of this study (provided we believe that a change in shedding mode may occur between Geometry 2 and 3, without direct experimental evidence), but would not be in agreement with the CFD data.

In the *transonic vortex shedding* phenomenon described by Melzer and Pullan [17] (see also Ref. [16])—a study conducted in parallel with the current work, and for the same purpose—the authors demonstrate (by means of unsteady Schlieren imaging) periodic shedding of pressure waves from the TE vortex structures. These pressure waves propagate away from the TE, and, in the case of the PS wave, impinge on the SS of the adjacent vane, stimulating rapid thickening of the boundary layer and additional total pressure loss. The primary component of the additional loss is not the direct result of the interaction of the strengthened vortex with the base region, but rather a secondary result of the pressure wave caused by the vortex impinging on the adjacent vane.

Considering this quantitatively, the corrected mixed-out average loss coefficient increase measured in experiment between

Fig. 19 (a) Normalized average base region pressures and (b) base pressure coefficients

Geometries 2 and 3 was +15.6% (Table 8) of ζ_1'''' (or, equivalently $\zeta_{1,\mathrm{corr}}''''$). This is 12.6% (of ζ_1'''') greater than the corresponding rise predicted by URANS. We believe that this difference may be substantially due to the inability of the URANS CFD method to accurately predict the effects arising from shed pressure waves associated with vortex shedding in the transonic range. This is broadly in accord with Melzer [16], who measured increases in mixed-out average KE loss coefficient of between 10% and 20% at transonic Mach numbers between cooled TE geometries which exhibited shed pressure waves associated with vortex shedding, and those which did not. We reinforce again that no direct evidence of a change in shedding mode was available in the experimental data of this study, but we propose that it is likely based on very similar trends analyzed in the experimental and time-averaged URANS data (analysis of Figs. 10, 12, and 14).

Noting that while the URANS method may be adequate for predicting the shedding mode shift (albeit at a slightly different SS-overhang length), it appears to be poor at accurately predicting shed pressure waves (see, e.g., Refs. [30,31]) and therefore the boundary layer interaction on the adjacent vane SS. This, in combination with the Melzer and Pullan [17] mechanism, seems a likely explanation for the differences in corrected mixed-out loss coefficient trend between experiment and CFD. A more sophisticated unsteady numerical method (i.e., large eddy simulations (LES)) would give greater insight into this theory, and we believe would likely close the gap.

Conclusions

In this article, we have studied the impact of TE overhang length on the aerodynamic performance of fully cooled transonic HP NGVs. High-fidelity experimental traverse measurements and unsteady numerical simulations were used for the study. Four different overhang lengths were tested. To account for differences in TE thickness between designs (an issue that has not been addressed in previous studies), a corrected mixed-out average KE loss coefficient was used as the representation of overall loss, where a correction for TE thickness was performed using a control volume method.

The key conclusions of the study are as follows:

(1) There was a large increase in the magnitude of unsteady pressure fluctuations in the base region when SS-overhang length became short, and a fall in shedding frequency. This was attributed to a change in vortex shedding mode, from one in which small vortices are shed at relatively high frequency from the extended SS TE tip, to one in which larger eddies are shed (at lower frequency) from the entire base region. There was conclusive evidence for this effect in the URANS simulations. Unsteady measurements were not available from the experiment; however, very similar changes (smaller spanwise fluctuations in radial profiles of local KE loss coefficient, and lower and broader peaks in circumferential profiles of local KE loss coefficient—characteristic of enhanced mixing close to the TE) were observed in the experimental data and time-averaged URANS data when overhang length became small. This led to the suggestion that this effect was likely also present in the experiment. The mode shift appears to have occurred at slightly longer overhang length in the experimental data than the CFD data.

(2) For both experiment and CFD, the longest overhang length tested (6.3% of tangential chord) gave the lowest corrected mixed-out average loss coefficient. The corrected mixed-out average loss coefficient for the centered-ejection type design was 22.1% greater than for the longest overhang in experiment, and 7.7% greater in CFD. This result supports the view that, for a typical engine component NGV operating at high-subsonic Mach number, SS-overhang designs generally provide an aerodynamic advantage over the centered-ejection design. In the engine design process, this

should be considered alongside the cooling requirements of different TE designs.

(3) URANS CFD predicted a gradual increase in corrected mixed-out average profile loss coefficient as overhang length was reduced, before plateauing at very short overhang length. The experimental data were largely in agreement with URANS in terms of the trend in mixed-out average profile loss coefficient between TE geometries, but showed an additional +12.6% increase in corrected mixed-out average loss coefficient at intermediate overhang lengths, which was not captured by the CFD. The discrepancy is thought to be caused by shed pressure waves associated with vortex shedding in the transonic range in the experimental data, which are not captured in the CFD simulations (a known limitation of the URANS method). The additional loss arises due to significant thickening of the SS boundary layer.

(4) Notwithstanding the boundary layer thickening effect associated with shed pressure waves in the experiment, we observe only small changes in boundary layer loss coefficient in the CFD data. Likewise, the impact of overhang length on secondary and endwall flows was shown to be small, and affected by changes in the precise geometry of the TE-endwall junction. The overall KE loss coefficient characteristic was therefore assumed to be dominated by changes in base pressure drag and aerodynamic changes in the vane passage.

(5) Analysis of the base region pressure distributions predicted by URANS shows a substantial fall in PS base region pressure with decreasing overhang length but very little sensitivity of the SS base region pressure. The different behaviors of the PS and SS base regions are explained by changes in the entire vane aerodynamics, associated with upstream migration of a low-pressure region. Interestingly, and contrary to some previous studies, there does *not* seem to be a simple relationship between changes in base region pressure and loss coefficient, suggesting that the overall loss cannot be understood without considering the aerodynamic change within the entire passage. This is an interesting area for future analysis.

(6) The mean exit whirl angle fell slightly as SS-overhang length was reduced (differences of up to 0.65 deg), due to a gradual reduction in the guided turning length provided by the SS-overhang.

Funding Data

Conflict of Interest

There are no conflicts of interest.

Data Availability Statement

The authors attest that all data for this study are included in the paper.

Nomenclature

k = total trailing edge blockage (defined in the Appendix), m
l = baseline suction-side trailing edge overhang length, m
p = static pressure, Pa
r = radius, m
s = vane pitch, m
t = trailing edge thickness, m
v = velocity, m/s
w = passage width, m
x = axial distance, m
y = distance in slot-normal direction, m
M = Mach number

F = isentropic capacity function
$\dot{m}$ = mass flowrate, kg/s
$\bar{p}$ = time-mean value of unsteady pressure signal, Pa
c_p = specific heat at constant pressure, J/kg/K
p_0 = stagnation pressure, Pa
$\overline{p_{02}}$ = plane-average downstream stagnation pressure, Pa
$\overline{p_{02}'}$ = mixed-out average downstream stagnation pressure, Pa
$\overline{p_2}$ = plane-average downstream static pressure, Pa
$\overline{p_2'}$ = mixed-out average downstream static pressure, Pa
$\overline{p_b}$ = average base region pressure, Pa
t_s = trailing edge slot width, m
M_2 = mean vane exit Mach number
C_{pb} = base pressure coefficient
C_x = axial chord length, m
C_θ = tangential chord length, m
T_0 = stagnation temperature, K
x' = true axial distance, m
Re = Reynolds number based on midspan tangential chord length, $\rho \bar{v} C_\theta / \mu$
St = Strouhal number
Tu = turbulence intensity, %

Greek Symbols

α = cascade stagger angle, deg
β = flow turning (or whirl) angle, deg
$\bar{\beta}$ = circumferential-average whirl angle, deg
γ = ratio of specific heats
δ = deviation angle, deg
δ^* = boundary layer displacement thickness, m
ζ = kinetic energy loss coefficient
ζ' = local kinetic energy loss coefficient
$\widehat{\zeta'}$ = peak local kinetic energy loss coefficient
ζ'' = circumferential-average kinetic energy loss coefficient at a particular radius
ζ''' = plane-average kinetic energy loss coefficient
ζ'''' = mixed-out average kinetic energy loss coefficient
ζ_1'''' = mixed-out average kinetic energy loss coefficient for Geometry 1
ζ_{BL}'''' = kinetic energy loss coefficient associated with boundary layer flows
ζ_{corr}'''' = corrected mixed-out average kinetic energy loss coefficient
ζ^* = kinetic energy loss coefficient resulting from the model in Appendix A
η = row efficiency
θ = normalized circumferential distance, vane pitches
θ^* = boundary layer momentum thickness, m
λ_2 = lambda-2 criterion
μ = dynamic viscosity, kg/m/s
ρ = mass density, kg/m^3
χ = $(\gamma-1)/\gamma$

Subscripts

0 = stagnation conditions
1 = vane inlet condition/TE Geometry 1
2 = vane exit condition/TE Geometry 2
3 = TE Geometry 3
4 = TE Geometry 4
c = coolant stream
m = mainstream
ref = reference condition for normalization
RMS = root-mean-square value
PS = pressure side
s = isentropic condition
SS = suction side
TE = trailing edge coolant stream

Appendix: Method for Loss Coefficient Scaling to Account for Trailing Edge Thickness

In this section, we apply a mass-momentum control volume method to determine a scale factor for the mixed-out average loss coefficient to correct the data for each particular TE design (and associated TE thickness) to a reference value of TE thickness. A method of this kind was first presented by Stewart [27] and has since appeared a number of times in the literature for the evaluation of mixing loss downstream of a vane cascade.

Figure 20(a) shows a control volume ABCDEFA bounding a region of flow downstream of a simplified representation of a staggered NGV cascade with solid (uncooled) TEs (see, e.g., Denton [32]). The flow at inlet to the control volume (AB) is considered to be uniform across the freestream region, with boundary layers characterized by total displacement and momentum thicknesses δ^* and θ^*, respectively. The exit flow (DE) is fully mixed out. The fluxes and pressures across the periodic boundaries (CD and AB) exactly cancel and can be neglected. Here—for simplicity—we assume an incompressible solution with zero deviation angle ($\delta = 0$): this avoids the need to estimate the suction surface pressure downstream of the throat (p_{SS}) and makes the mixed-out average loss coefficient independent of the cascade stagger angle [32]. The resulting mixed-out average total pressure loss coefficient is given by

$$\frac{p_{01} - p_{02}}{\frac{1}{2}\rho v_1^2} = \left(\frac{t + \delta^*}{s\cos\alpha}\right)^2 + \frac{2\theta^*}{s\cos\alpha} - \frac{tC_{pb}}{s\cos\alpha} \quad \text{(A1)}$$

where C_{pb} is the base pressure coefficient, defined as follows:

$$C_{pb} = \frac{p_b - p_1}{\frac{1}{2}\rho v_1^2} \quad \text{(A2)}$$
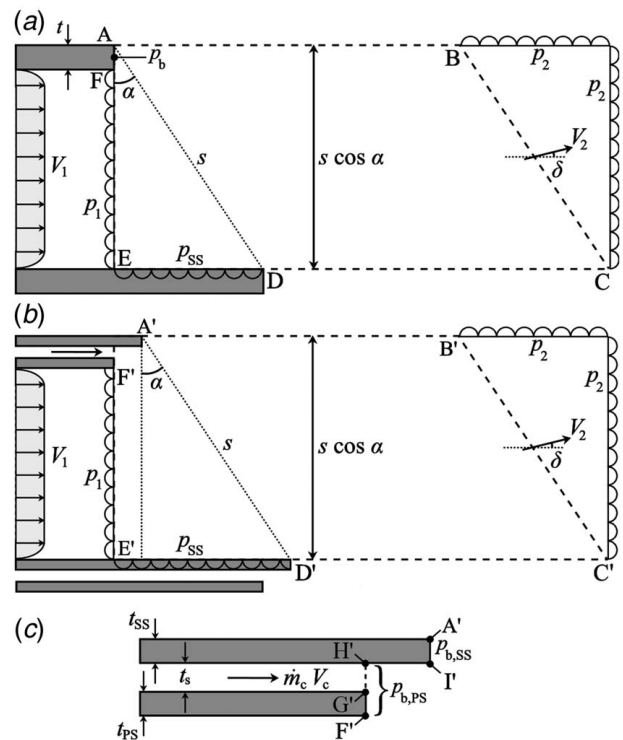

Fig. 20 Control volumes for the wake mixing processes downstream of (a) a staggered cascade with a solid TE, (b) a staggered cascade with a TE slot, and (c) inset diagram of the TE geometry for the control volume in (b)

The first term on the right-hand side in Eq. (A1) represents the loss due to the total blockage of the TE and surface boundary layers. The second term represents the mixed-out average loss coefficient of the boundary layers at the TE, and the third term represents the base pressure loss.

Figure 20(b) shows an adapted control volume in which the solid TE is replaced by separate SS and PS lands, separated by a TE slot, and with an SS-overhang of arbitrary length. A close view of the TE geometry is shown in Fig. 20(c). The adapted control volume is A′B′C′D′E′F′G′H′I′A′.

In the real cascade, there is a complex static pressure distribution around the base region (see Fig. 18). In a complete solution, we would integrate this pressure distribution around the path F′G′H′I′A′ to determine the pressure force arising from this control volume boundary. For the purpose of this analysis, however, we define a simplified base region pressure distribution in which a uniform pressure $p_{b,SS}$ acts on the SS TE (A′I′), and a uniform pressure $p_{b,PS}$ acts on the PS TE and the TE slot exit (F′H′). This is justified on the basis that it provides a reasonable first approximation to the base region pressure distributions shown in Fig. 18. For each of TE Geometries 1–4, we set the values of $p_{b,SS}$ and $p_{b,PS}$ to the CFD-predicted average base region pressures shown in Fig. 19(a). The pressure force on the inner surface of the SS-overhang (H′I′) has no component in the x-direction and is therefore not required in the case that $\delta = 0$.

We now derive an incompressible solution for the mixed-out average loss coefficient of the adapted scenario (represented in Fig. 20(b)). First applying conservation of mass

$$\rho V_1(s \cos \alpha - k) + \rho V_c t_s = \rho V_2 s \cos(\alpha - \delta) \quad \text{(A3)}$$

where k is the total TE blockage given by $k = t_{SS} + t_{PS} + t_s + \delta^*$. Then by applying conservation of momentum in the x-direction,

$$\dot{m}_m V_1\left(1 - \frac{\theta^*}{s \cos \alpha - k}\right) + \dot{m}_c V_c - (\dot{m}_m + \dot{m}_c)V_2 \cos \delta$$
$$= p_2 s \cos \alpha - p_1(s \cos \alpha - t_{SS} - t_{PS} - t_s)$$
$$- p_{b,SS} t_{SS} - p_{b,PS}(t_{PS} + t_s) \quad \text{(A4)}$$

Then, taking the assumption that $\delta = 0$ (to simplify the analysis), replacing the mass flowrates $\dot{m}_m$, $\dot{m}_c$, and $(\dot{m}_m + \dot{m}_c)$ in Eq. (A4), with the equivalent terms from Eq. (A3), and rearranging, we obtain

$$p_1 - p_2 = \frac{\rho V_2^2 - \rho V_1^2\left(1 - \frac{k + \theta^*}{s \cos \alpha}\right) - \rho V_c^2 \frac{t_s}{s \cos \alpha}}{-(p_{b,SS} - p_1)\frac{t_{SS}}{s \cos \alpha} - (p_{b,PS} - p_1)\frac{(t_{PS} + t_s)}{s \cos \alpha}} \quad \text{(A5)}$$

A total pressure loss coefficient is derived from the incompressible relations between total and static pressure:

$$\frac{p_{01} - p_{02}}{1/2 \rho V_1^2} = \frac{p_1 - p_2 + 1/2\rho V_1^2 - 1/2\rho V_2^2}{1/2\rho V_1^2} \quad \text{(A6)}$$

then by substituting for $p_1 - p_2$ using Eq. (A5) and simplifying, we obtain

$$\frac{p_{01} - p_{02}}{1/2\rho V_1^2} = \left(\frac{V_2}{V_1}\right)^2 - 1 + \frac{2k}{s \cos a} + \frac{2\theta^*}{s \cos a}$$
$$- 2\left(\frac{V_c}{V_1}\right)^2 \frac{t_S}{s \cos a} - C_{pb,SS}\frac{t_{ss}}{s \cos a} - C_{pb,PS}\frac{(t_{PS} + t_s)}{s \cos a} \quad \text{(A7)}$$

where

$$C_{pb,SS} = \frac{p_{b,SS} - p_1}{1/2\rho V_1^2} \quad \text{(A8)}$$

and

$$C_{pb,PS} = \frac{p_{b,PS} - p_1}{1/2\rho V_1^2} \quad \text{(A9)}$$

By using the continuity Eq. (A3), we can obtain expressions for the velocity ratios V_2/V_1 and V_c/V_1, as follows:

$$\frac{V_2}{V_1} = \left(1 - \frac{k}{s \cos \alpha}\right)\left(1 + \frac{\dot{m}_c}{\dot{m}_m}\right) \quad \text{(A10)}$$

$$\frac{V_c}{V_1} = \frac{(s \cos \alpha - k)}{t_s}\frac{\dot{m}_c}{\dot{m}_m} \quad \text{(A11)}$$

By substituting Eqs. (A10) and (A11) into Eq. (A7), we obtain

$$\frac{p_{01} - p_{02}}{\frac{1}{2}\rho v_1^2} = \left(1 - \frac{2k}{s \cos \alpha}\right)\left(2 + \frac{\dot{m}_c}{\dot{m}_m}\right)\frac{\dot{m}_c}{\dot{m}_m} + \frac{2\theta^*}{s \cos \alpha}$$
$$+ \left(\frac{k}{s \cos \alpha}\right)^2\left(1 + \frac{\dot{m}_c}{\dot{m}_m}\right)^2 + \frac{2(s \cos \alpha - k)^2}{t_s s \cos \alpha}\left(\frac{\dot{m}_c}{\dot{m}_m}\right)^2$$
$$- \frac{t_{SS} C_{pb,SS}}{s \cos \alpha} - \frac{(t_{PS} + t_s)C_{pb,PS}}{s \cos \alpha} \quad \text{(A12)}$$

Let us consider the right-hand side of Eq. (A12). The second term is unchanged from Eq. (A1); the final two terms represent the base pressure term from Eq. (A1) split into separate SS and PS parts; the remaining terms represent the total blockage effect of the entire base region, as well as the mixing of the TE coolant flow with the mainstream.

The mixed-out average total pressure, p_{02}, was estimated using Eq. (A12) and used to determine a corresponding KE loss coefficient according to Eq. (5).

Consider now an adaptation of this theory to compressible flow. Denton and Xu [1] presented a compressible flow solution for the model of Fig. 20(a). Deckers and Denton [28] extended the analysis to include coolant ejection from a TE slot. A very similar solution procedure was followed in the present study, adapted to represent the model of Fig. 20(b).

We now express the mainstream mass flowrate at the TE (station 1), and the mixed-out mass flowrate at station 2, using the isentropic capacity function:

$$\frac{\dot{m}_m \sqrt{c_p T_{01}}}{p_{01}(s \cos \alpha - k)} = F(M_1, \gamma) \quad \text{(A13)}$$

$$\frac{(\dot{m}_m + \dot{m}_c)\sqrt{c_p T_{02}}}{p_{02}s \cos(\alpha - \delta)} = F(M_2, \gamma) \quad \text{(A14)}$$

where

$$F(M, \gamma) = \frac{\gamma}{\sqrt{\gamma - 1}} M\left(1 + \frac{\gamma - 1}{2}M^2\right)^{\frac{\gamma + 1}{2(1 - \gamma)}} \quad \text{for all } M \le 1 \quad \text{(A15)}$$

Combining Eqs. (A13) and (A14) gives the mixed-out average total pressure:

$$\frac{p_{02}}{p_{01}} = \left(1 + \frac{\dot{m}_c}{\dot{m}_m}\right)\sqrt{\frac{T_{02}}{T_{01}}}\frac{(s \cos \alpha - k)}{s \cos(\alpha - \delta)}\frac{F(M_1)}{F(M_2)} \quad \text{(A16)}$$

We consider the isothermal case $T_{02} = T_{01}$, but more generally, T_{02} can be calculated using the energy equation. Again, we make the assumption that $\delta = 0$ to simplify the analysis. We then simultaneously solve Eq. (A16) and the momentum equation in the x-direction, Eq. (A4) (which remains valid for compressible flow conditions), for the mixed-out average Mach number, M_2, and the mixed-out average total pressure, p_{02}, using an iterative process. The mixed-out Mach number, M_2, was iteratively changed, and the corresponding mixed-out conditions of total and static pressure updated using Eq. (A16), until the sum of the base pressure terms, $C_{pb,SS}t_{SS}/(s \cos \alpha) + C_{pb,PS}(t_{PS} + t_s)/(s \cos \alpha)$, in Eq. (A4) was equal to the value indicated by the CFD results. This differs from the process proposed in Ref. [28] in that known (or predicted) base pressures are used to set the target for the iterative process, rather than being a secondary output from the calculation. We note
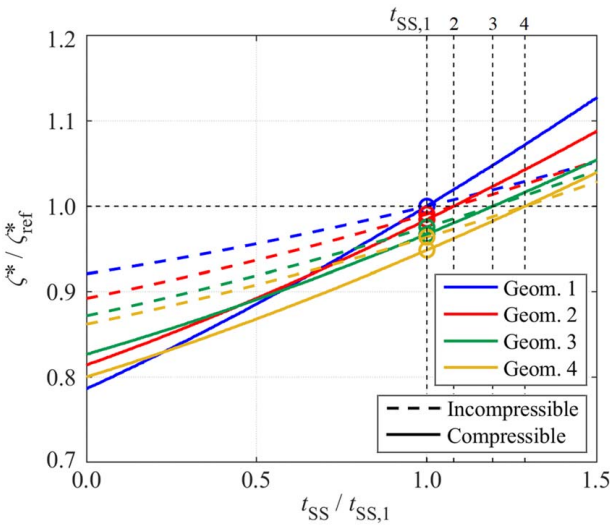
Fig. 21 Normalized KE loss coefficient as a function of t_{SS}, for each TE geometry

again that base pressure data were available only from the CFD study. Therefore, it was necessary to assume that the CFD-predicted base pressure values for each TE overhang length were approximately applicable to the equivalent experiment at the same vane pressure ratio.

Both the incompressible (Eq. (A12)) and compressible (the iterative process described) models were used to estimate mixed-out average total pressure, p_{02}, as a function of SS TE thickness, t_{SS}, for each of the four TE geometries tested in this article (i.e., using base pressure values that approximated the base region pressure distributions in each case, and running the calculation for a range of t_{SS} values). KE loss coefficient, ζ (Eq. (1)), was then calculated as a function of t_{SS} for each geometry. This leads to four characteristics: ζ_1^* to ζ_4^*. The values of these characteristics at their respective nominal SS TE thicknesses, $t_{SS,1}$ to $t_{SS,4}$, are referred to as the reference values $\zeta_{1,ref}^*$ to $\zeta_{4,ref}^*$. We plot the normalized characteristics $\zeta_1^*/\zeta_{1,ref}^*$ to $\zeta_4^*/\zeta_{4,ref}^*$ in Fig. 21. Plotted in this way, the normalized characteristics pass through unity at the nominal SS TE thickness for that particular geometry.

The abscissa shows t_{SS} normalized with respect to the value for Geometry 1, $t_{SS,1}$. $t_{SS,1}$ is the SS TE thickness, which we wish to scale the loss coefficient values for all TE geometries *to* and is indicated by the left-most vertical dashed line in Fig. 21. The other three vertical dashed lines indicate the nominal t_{SS} values for Geometries 2–4.

For all geometries, ζ^*/ζ_{ref}^* continuously increases with t_{SS} as expected (rise in TE blockage), and the gradient steadily increases with t_{SS} (in line with Eq. (A12), which shows that the loss due to TE blockage is quadratic in TE thickness).

The scaling factors to correct the loss coefficient for each TE geometry from their uncorrected (i.e., at $t_{SS,n}$ value) to their estimated value at thickness $t_{SS,1}$ are read from the ordinate value at which each curve intersects the vertical line $t_{SS} = t_{SS,1}$. These points are marked with circles in Fig. 21. We obtain scale factors 0.991, 0.976, and 0.964 using the incompressible model, and 0.985, 0.967, and 0.949 using the compressible model, for Geometries 2, 3, and 4, respectively (the scale factor for Geometry 1 is unity by definition). These values are summarized in Table 7. We note that these scaling functions are intended for correcting for relatively small differences in t_{SS} between our geometries, not for accurate prediction of absolute values of loss coefficient.

References

[1] Denton, J. D., and Xu, L., 1990, "The Trailing Edge Loss of Transonic Turbine Blades," ASME J. Turbomach., **112**(2), pp. 277–285.

[2] Reeman, J., and Simonis, E. A., 1943, "The Effect of Trailing Edge Thickness on Blade Loss," RAE Technical Note Eng. 116.

[3] Johnston, I. H., Dransfield, D. C., and Fullbrook, D. J., 1967, "Experiments Concerning the Effect of Trailing Edge Thickness on Blade Loss and Turbine Stage Efficiency," Ministry of Aviation Aeronautical Research Council Reports and Memoranda No. 3459.

[4] Whitney, W. J., Szanca, E. M., and Behning, F. P., 1969, "Cold-Air Investigation of a Turbine With Stator-Blade Trailing-Edge Coolant Ejection: Part I—Overall Stator Performance," NASA Technical Memorandum X-1901.

[5] Prust, H. W., and Bartlett, W. M., 1974, "Cold-Air Study of the Effect on Turbine Stator Blade Aerodynamic Performance of Coolant Ejection From Various Trailing-Edge Slot Geometries: Part I–Experimental Results," NASA Technical Memorandum X-3000.

[6] Prust, H. W., 1975, "Cold-Air Study of the Effect on Turbine Stator Blade Aerodynamic Performance of Coolant Ejection From Various Trailing-Edge Slot Geometries: Part II–Comparison of Experimental and Analytical Results," NASA Technical Memorandum X-3190.

[7] Sieverding, C. H., 1982, "The Influence of Trailing Edge Ejection on the Base Pressure in Transonic Turbine Cascades," Proceedings of ASME 1982 International Gas Turbine Conference and Exhibit, London, UK, Apr. 18–22, Paper No. 82-GT-50.

[8] Kost, F., and Holmes, A., 1985, "Aerodynamic Effect of Coolant Ejection in the Rear Part of Transonic Rotor Blades," AGARD-CP-390, Heat Transfer and Cooling in Gas Turbine Blades, Paper 41.

[9] Raffel, M., and Kost, F., 1998, "Investigation of Aerodynamic Effects of Coolant Ejection at the Trailing Edge of a Turbine Blade Model by PIV and Pressure Measurements," Exp. Fluids, **24**(5–6), pp. 447–461.

[10] Pappu, K. R., and Schobeiri, M. T., 1999, "Optimization of Trailing Edge Ejection Mixing Losses: A Theoretical and Experimental Study," ASME J. Fluids Eng., **121**(1), pp. 118–125.

[11] Montis, M., Niehuis, R., Guidi, M., Salvadori, S., Martelli, F., and Stephan, B., 2009, "Experimental and Numerical Investigation on the Influence of Trailing Edge Bleeding on the Aerodynamics of a NGV Cascade," Proceedings of ASME Turbo Expo 2009, Orlando, FL, June 8–12, Paper No. GT2009-59910.

[12] Rehder, H. J., 2012, "Investigation of Trailing Edge Cooling Concepts in a High Pressure Turbine Cascade: Aerodynamic Experiments and Loss Analysis," ASME J. Turbomach., **134**(5), p. 051029.

[13] Wang, Y., Zhou, X., Liu, X., and Wang, S., 2016, "Influence of Trailing Edge Coolant Ejection Rate and Cut-Back Length on Energy Loss and Shockwave Intensity of a Transonic Turbine Blade," Proceedings of ASME Turbo Expo 2016, Seoul, Korea, June 13–17, Paper No. GT2016-56859.

[14] Kapteijn, C., Amecke, J., and Michelassi, V., 1994, "Aerodynamic Performance of a Transonic Turbine Guide Vane With Trailing Edge Coolant Ejection: Part I —Experimental Approach," Proceedings of ASME 1994 International Gas Turbine and Aeroengine Congress and Exposition, Den Haag, Netherlands, June 13–16, Paper No. 94-GT-288, p. V001T01A099.

[15] Uzol, O., and Camcı, C., 2001, "Aerodynamic Loss Characteristics of a Turbine Blade With Trailing Edge Coolant Ejection: Part II—External Aerodynamics, Total Pressure Losses and Predictions," ASME J. Turbomach., **123**(2), pp. 249–257.

[16] Melzer, A., 2018, "Aerodynamics of Transonic Turbine Trailing Edges," Ph.D. thesis, University of Cambridge, Cambridge, UK.

[17] Melzer, A. P., and Pullan, G., 2019, "The Role of Vortex Shedding in the Trailing Edge Loss of Transonic Turbine Blades," ASME J. Turbomach., **141**(4), p. 041001.

[18] Kirollos, B., Lubbock, R., Beard, P., Goenaga, F., Rawlinson, A., Janke, E., and Povey, T., 2017, "ECAT: An Engine Component Aerothermal Facility at the University of Oxford," Proceedings of ASME Turbo Expo 2017, Charlotte, NC, June 26–30, Paper No. GT2017-64736.

[19] Burdett, D., Hambidge, C., and Povey, T., 2020, "Analysis of Ultra-Low Uncertainty Gas Turbine Flow Capacity Measurement Techniques," Proc. Inst. Mech. Eng. Part A J. Power Energy, **235**(5), pp. 1053–1079.

[20] Burdett, D., and Povey, T., 2022, "Experimental and Numerical Analysis of Loss Characteristics of Cooled Transonic Nozzle Guide Vanes," ASME J. Turbomach., **144**(5), p. 051009.

[21] Day, C. R. B., Oldfield, M. L. G., and Lock, G. D., 2000, "Aerodynamic Performance of an Annular Cascade of Film Cooled Nozzle Guide Vanes Under Engine Representative Conditions," Exp. Fluids, **29**(2), pp. 117–129.

[22] Burdett, D., Lubbock, R., and Povey, T., 2018, "An Impulse Response Technique to Improve the Effective Frequency Response of Pressure Probes," XXIV Biennial Symposium on Measuring Techniques in Turbomachinery, Prague, Czech Republic, Aug. 29–31, Paper No. MTT2418B23.

[23] Burdett, D., and Povey, T., 2022, "Analysis of Averaging Methods for Non-Uniform Total Pressure Fields," ASME J. Turbomach., **144**(5), p. 051011.

[24] Dzung, L. S., 1971, "Konsistente Mittlewerte in der Theorie der Turbomaschinen für Kompressible Medien," BBC-Mitt., **58**, pp. 485–492.

[25] Burdett, D., Goenaga, F., and Povey, T., 2021, "Impact of Trailing Edge Geometry on the Flow Capacity of Transonic Turbine Nozzle Guide Vanes," ASME J. Turbomach., **143**(5), p. 051001.

[26] Blevins, R. D., 1990, *Flow-Induced Vibration*, 2nd ed., Van Nostrand Reinhold Co. Inc., New York.

[27] Stewart, W. L., 1955, "Analysis of Two-Dimensional Compressible-Flow Loss Characteristics Downstream of Turbomachine Blade Rows in Terms of Basic Boundary Layer Characteristics," NACA Technical Note 3515.1955.

[28] Deckers, M., and Denton, J. D., 1997, "The Aerodynamics of Trailing-Edge-Cooled Transonic Turbine Blades: Part 2—Theoretical and

Computational Approach," Proceedings of ASME International Gas Turbine and Aeroengine Congress and Exhibition 1997, Orlando, FL, June 2–5, Paper No. 97-GT-519.

[29] Mee, D. J., Baines, N. C., Oldfield, M. L. G., and Dickens, T. E., 1990, "An Examination of the Contributions to Loss on a Transonic Turbine Blade in Cascade," ASME J.Turbomach., **114**(1), pp. 155–162.

[30] Léonard, T., Gicquel, L. Y. M., Gourdain, N., and Duchaine, F., 2015, "Steady/ Unsteady Reynolds-Averaged Navier-Stokes and Large Eddy Simulations of a Turbine Blade at High Subsonic Outlet Mach Number," ASME J. Turbomach., **137**(4), p. 041001.

[31] Lin, D., Su, X., and Yuan, X., 2018, "The Development and Mechanisms of the High Pressure Turbine Vane Wake Vortex," ASME J. Eng. Gas Turbines Power, **140**(9), p. 092601.

[32] Denton, J. D., 1993, "Loss Mechanisms in Turbomachines," Proceedings of ASME 1993 International Gas Turbine and Aeroengine Congress and Exposition, Cincinnati, OH, May 24–27, Paper No. 93-GT-435, p. V002T14A001.